UiT The Arctic University of Norway

Faculty of Science and Technology
Department of Physics and Technology

The effects of time-variation of electron fluxes from the auroral ionosphere on M-I coupling

Etienne Gavazzi

FYS-3900 Master's thesis in physics - 60 ECTS
15 May 2022

This thesis document was typeset using the *UiT Thesis LaTeX Template*.
© 2022 – http://github.com/egraff/uit-thesis

Abstract

Electric potential-differences between the magnetospheric and the ionospheric end of a magnetic flux tube lead to the downward acceleration of electrons in the ionosphere, producing visible auroral arcs. Most of the potential-drop is situated in a narrow altitude-region known as double layer. In the ionosphere, the precipitation of high-energy electrons will produce secondary electrons. Some of the primary and secondary electrons will escape out of the ionosphere back up along the magnetic flux tube. In this work, we study the dynamic effects from the onset of upward-streaming electrons from the ionosphere on a double layer potential structure situated in the acceleration region.

We find that the onset of the upward-streaming electrons is the source of perturbations in the electric field between the double layer and the ionosphere. The perturbations do not seem to affect the structure of the double layer, but have an effect on the precipitation of electrons.

Acknowledgements

The realisation of this thesis would not have been possible without the help and support of my supervisor Björn Gustavsson. Thank you for introducing me to this subject, for the many scientific discussions and for your precious insights and feedback on this thesis. I also appreciate your efforts trying to expand my knowledge of classical Swedish culture.

I would like also to thank the master students sharing office with me for keeping the spirits up the whole year, and especially during those last weeks.

I am also grateful to my family, to my friends, and particularly to my girlfriend Amanda for their continuous support during my studies and through this thesis.

Finally, thank you to the people of the Complex System Modelling group who have accepted a space physicist among theirs. The cakes have been of great help to this work.

Contents

Abstract **i**

Acknowledgements **iii**

List of Figures **vii**

List of Tables **ix**

1 Introduction **1**
- 1.1 Thesis structure 4

2 Vlasov simulations of double layers **7**
- 2.1 Electrostatic Vlasov-Maxwell equation 8
- 2.2 Important parameters 11
  - 2.2.1 Densities at the boundaries 11
  - 2.2.2 Magnetic field configuration 12
  - 2.2.3 Dielectric constant 13

3 Ionospheric electron-transport model **15**
- 3.1 Transport equation 16
- 3.2 Numerical implementation 22
  - 3.2.1 Energy discretization 22
  - 3.2.2 Pitch-angle discretization 23
  - 3.2.3 Crank-Nicolson scheme 23

4 Magnetosphere - Ionosphere coupling **33**
- 4.1 Protocol 33
- 4.2 Transition altitude 35
- 4.3 Conversions of distribution functions and fluxes 35

5 Results **41**

6 Discussions **49**

List of Figures

1.1 Magnetospheric regions of interest 2
1.2 U-shaped potential structure 4

2.1 Geometry of the model 9

3.1 Velocity coordinate systems 17
3.2 Stencil of our Crank-Nicolson scheme 25
3.3 Differences between CFL64 and CFL1 32

4.1 Electron fluxes through the ionosphere 36
4.2 Change of velocity grids 38
4.3 Refining the velocity grid 39

5.1 E-field and potential for steady-state conditions 43
5.2 z-t diagram of the electric field for steady-state conditions . . 43
5.3 Fluxes in and out of the ionosphere for the different runs . . 44
5.4 Absolute difference between the fluxes in and out of the ionosphere from the 3rd and 4th run. 45
5.5 Energy-time diagrams of the fluxes at the top of the ionosphere for different pitch-angles 45
5.6 z-t diagrams of the electric field for the different runs 47

List of Tables

4.1 Proportion of electron flux changing bin after a back and forth change of grid, as a function of the width of the θ bins . . . 40

5.1 Boundary conditions of our acceleration region 42

1

Introduction

The aurora is the optical manifestation of a complex underlying system of interactions between the solar wind, the magnetosphere and the ionosphere. The many different observable auroral events, such as discrete auroral arcs, diffuse aurora, flickering aurora, ... are just as many different interaction processes at work. In this thesis, we interest ourselves to the onset of the most common and characteristic type of auroral event, quiescent discrete auroral arcs. These arcs can be stable from minutes to hours and are associated with relatively stable magnetotail conditions, in comparison to substorm breakups.

Several mechanisms are at the origin of quiescent discrete auroral arcs. Along one magnetic field line, they can be grouped into three regions (e.g. Birn et al., 2012; Borovsky et al., 2019; Lysak et al., 2020) : the generator region, the acceleration region and the ionospheric dissipation region (see figure 1.1). In this system, the generator and acceleration mechanisms are the less fully understood and are still very active fields of research in space physics. The main reason for our relatively poor understanding of these two regions is their size, spanning several earth radius. This makes extensive spatio-temporal measurements by satellites difficult if not impossible regarding the current missions in orbit.

In this thesis, we will not venture into the physics of the generator mechanisms, driven mainly by interactions between the solar wind and the magnetosphere. For this part of the global system, we can recommend the review of magnetospheric generator mechanisms by Borovsky et al. (2019). Just note that it

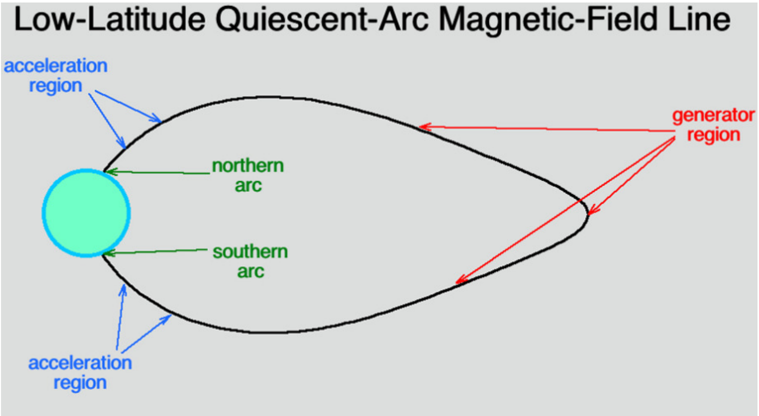

Figure 1.1: Sketch of the position of the three key regions along one magnetic field line. The northern and southern auroral arc are the visible effect of the dissipation of particle's energy in the ionosphere. (From Borovsky et al., 2019).

has been convincingly argued that it is unlikely for the generator of quiescent auroral arcs to be situated beyond 15 Re in the equatorial region of the magnetotail, as this region is way too dynamic to drive stable auroral arcs (Borovsky et al., 2019). Instead, we will focus on the auroral acceleration mechanisms. These mechanisms are responsible for the acceleration of electrons, primarily from the plasma sheet with typical temperatures of a few 100 eV, to auroral energies of several keV. They are often the result of some underlying magnetosphere-ionosphere (M-I) coupling (e.g. De Keyser and Echim, 2010 ; Lysak et al., 2020).

One of the key mechanism commonly recognised as responsible for the acceleration of auroral particles are electric fields parallel to the magnetic field lines. This mechanism was first suggested by Alfvén (1958) and has seen an important development after the first particle observations from polar orbiting satellites flying across magnetic field lines. Under discrete auroral arc conditions, measurements show inverted-V like structures in energy-time spectrograms. This is a strong hint for an acceleration from quasi-static parallel electric fields, as a U-shaped potential structure (see figure 1.2) along the magnetic field line can explain the linear rise to a peak energy followed by a linear decrease. This can be confusing for anyone being introduced to the auroral acceleration region, as one can think that the large mobility of electrons and ions along magnetic field lines should rapidly neutralise any electric charge imbalance at the origin of the electric field structures. However, in recent years, more observations came to support the presence of quasi-static parallel electric fields (see section 6 of Lysak et al., 2020; G. T. Marklund, 1997; G. Marklund et al., 2002, 2007), and different models have been developed that can explain the formation of such structures along magnetic field lines.

Among those models, three candidates have stood out over the last years, all of which have received experimental support (Birn et al., 2012): large scale parallel electric fields, confined electric fields (known as double layers) and Alfvénic supported electric fields. Large scale parallel electric fields could form due to interactions between the magnetic mirroring structure and the flow of electrons and ions, creating anisotropy in their distributions along the field lines leading to large scale potential structures. Double layers correspond to small scale electric-potential structures, with size inferior to the local Debye length, allowing for the presence of two layers of net opposite charge while being globally neutral on a larger scale. Double layers could form at the interface between plasmas with different macroscopic properties, such as ionospheric and magnetospheric plasmas (Lysak et al., 2020). Finally, Alfvénic driven electric fields correspond to parallel electric fields carried by dispersive Alfvén waves. These are often associated with dynamic aurora, but as explained by Lysak et al. (2020): "while Alfvenic acceleration processes will likely play a role in more dynamic auroral structures, it can also be associated with field line resonances that have periods of minutes, and so the resulting auroral structures will appear to be quasi-static". For a more thorough description of those models, we can recommend the reviews on acceleration mechanisms by Birn et al. (2012) and Lysak et al. (2020). Note that even though the models are often developed independently and presented as such, the physical reality of the acceleration region might well be a combination of them to different degrees depending on the magnetospheric and ionospheric conditions.

As noted above, observing the acceleration mechanisms is a hard task. For this reason, the testing and refining of the different parallel electric field models relies heavily on numerical simulations. Among the numerical and theoretical tools at our disposal, nearly all rely either on a kinetic approach (Vlasov) or a magnetohydrodynamic approach (MHD) of the plasma dynamics. Kinetic Vlasov treatments give a complete description of the interactions between plasmas and parallel electric fields due to potential drops, but can be challenging to implement to include electromagnetic effects such as Alfvén waves. On the other hand, MHD treatments can be very useful to study Alfvénic effects in the magnetosphere, but cannot properly simulate potential drops at the origin of quasi-static electric fields. Either approach, the numerical simulations take into account the coupling between the ionosphere and the magnetosphere, as its effects are determining in all acceleration models. However, how accurately the ionospheric dissipation region is treated tends to vary between different simulation models. Often, the ionospheric end that is used is rather simple, both because of the complexity of taking into account a more accurate ionosphere, as the physical processes to model are of a different nature, and because the effects of a more accurate ionosphere are considered negligible, making the

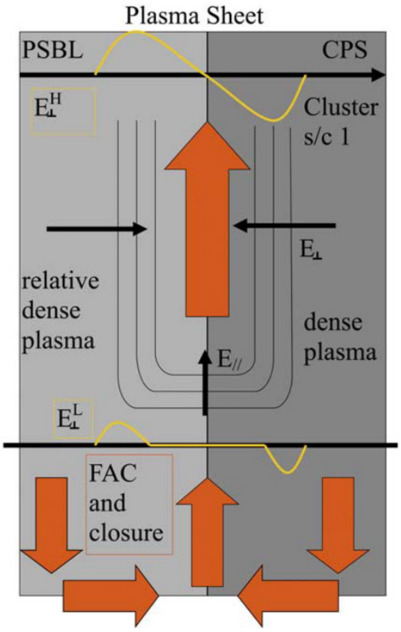

Figure 1.2: Diagram of the U-shaped potential structure behind quasi-static parallel electric fields. (From G. Marklund et al., 2007).

current level of accuracy satisfying.

The idea of this thesis is to take an electrostatic Vlasov-Maxwell simulation of double layers currently not using any ionospheric response, and to connect it with a time-dependent ionospheric model. This to investigate the possible effects of the ionospheric response on the acceleration region.

1.1 Thesis structure

In chapter 2, we describe the Vlasov simulation model of double layers by Gunell et al. (2013) that we are using. We review the theory behind the simulation in 2.1, before explaining the importance of some specific parameters of the model in 2.2.

Then, in chapter 3, we present the time-dependent ionospheric electron-transport model from Gustavsson (2022, accepted for publication in JGR). We derive the time-dependent electron-transport equation in 3.1, and describe its numerical implementation in 3.2.

Chapter 4 describes the methodology of our experiment connecting the two models.

In chapter 5, we present the results from our experiment, before discussing them in chapter 6.

2

Vlasov simulations of double layers

The coupled Vlasov-Maxwell system of equations give the most complete and self-consistent description of collision-less plasmas. The phase-space densities of the charged particles are modeled with the Vlasov equation using the electric and magnetic fields that are simultaneously solved with the Maxwell equations, using the currents and charge densities obtained from the phase-space densities. A problem with implementing numerically the coupled Vlasov-Maxwell system of equations is that the Debye length and plasma period are quite small, requiring extremely fine space and time grids demanding unreasonable computing power. For this reason, most Vlasov approaches solve time-independent situations (e.g. Echim et al., 2007), making abstraction of the time-grid. However, Gunell et al. (2013) have managed to develop a time-dependent Vlasov code using a trick we describe in section 2.2.3, allowing for coarser space-time grids and reasonable computing time. The power of a time-dependent Vlasov simulation is to make it possible to study the stability and lifetime of structures, such as double layers. To simulate double layers, a potential and plasma distributions are applied at both ends of a magnetic flux tube, and the behavior of the plasma species and the potential are simulated by solving the Vlasov equation.

The code of the model can be found at https://github.com/egavazzi/ketchup.

2.1 Electrostatic Vlasov-Maxwell equation

The core of the model of Gunell et al. (2013) is the electrostatic Vlasov-Maxwell equation along a magnetic field flux tube. As it is electrostatic, it will not account for electromagnetic effects such as Alfvén waves. The Vlasov equation corresponds to the Boltzmann equation where binary collisions are neglected, which is a good approximation when considering plasmas in the magnetosphere, where collisions frequencies are negligible. This means that the equation for phase-space density evolution (Boltzmann equation) simplifies to:

$$\frac{Df(\boldsymbol{r},\mathbf{v},t)}{Dt} = \left(\frac{\partial f(\boldsymbol{r},\mathbf{v},t)}{\partial t}\right)_{coll} = 0. \tag{2.1}$$

By placing ourselves in the center of the electrical potential structure where the perpendicular electric field is zero, the motion of particles happens only along the magnetic field line, which allows us to use only one spatial dimension z (see figure 2.1a). Then, we can decompose the velocity into a parallel velocity component v_z and a perpendicular velocity component $v_\perp$. This perpendicular velocity coordinate can also be written as the magnetic moment $\mu = \frac{mv_\perp^2}{2B(z)}$. The equation (2.1) for $f(z, v_z, \mu, t)$ then becomes

$$\begin{aligned} &\frac{\partial f}{\partial t} + \frac{\partial f}{\partial z}\frac{dz}{dt} + \frac{\partial f}{\partial v_z}\frac{dv_z}{dt} + \frac{\partial f}{\partial \mu}\cancelto{0}{\frac{d\mu}{dt}} = 0 \\ \Rightarrow &\frac{\partial f}{\partial t} + v_z\frac{\partial f}{\partial z} + \frac{1}{m}\left(qE_z - \mu\frac{dB}{dz} + ma_g\right)\frac{\partial f}{\partial v_z} = 0 \end{aligned} \tag{2.2}$$

where we have used that the magnetic moment μ is a constant of motion and Newton's second law to express dv_z/dt. The term $\mu dB/dz$ is the contribution from the magnetic mirror force. As we have made the electrostatic simplification, the magnetic field will be constant over time ($\boldsymbol{\nabla} \times \boldsymbol{E} = -\partial \boldsymbol{B}/\partial t = 0$) and we just need to choose an arc geometry to solve this term. The term ma_g is the contribution from the gravitational force. It can be easily derived given the arc geometry and the position along this arc. The term qE_z is the only remaining contribution from the Lorentz force. This is the challenging factor, since it is itself influenced by the motion of particles we describe with equation (2.2). The electric field is described by Gauss's law

$$\boldsymbol{\nabla} \cdot \boldsymbol{E} = \frac{\rho}{\epsilon} \tag{2.3}$$

where ρ is the charge density (in C/m^3) and ϵ the dielectric constant. Integrated over a flux segment of volume V, it becomes

$$\iiint_V \boldsymbol{\nabla} \cdot \boldsymbol{E} = \frac{Q}{\epsilon} \tag{2.4}$$

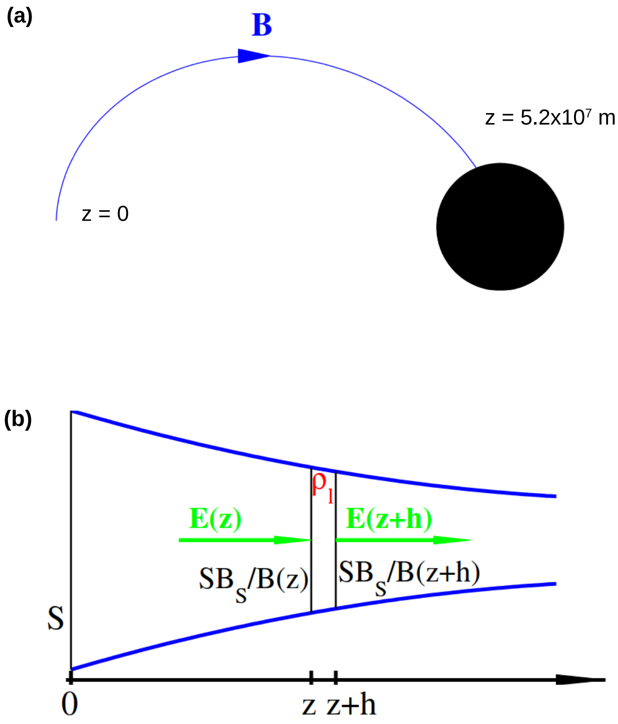

Figure 2.1: Geometry of the double layer model. **(a)** The magnetic field line along which the system is modelled. Altitude $z = 0$ corresponds to the magnetospheric end of the system, and $z = 5.2 \times 10^7$ m corresponds to the ionospheric end. **(b)** 2D profile of the magnetic flux tube. The blue curves represent the edges of the tube. The cross section of the flux tube at the magnetospheric end is equal to S. As the altitude z increases, the magnetic field $B(z)$ becomes stronger and the cross section given by $SB_S/B(z)$ becomes smaller. The length of a segment of flux tube is noted h, and ρ_l is the charge per unit length of flux tube (in C/m). (Adapted from Gunell et al., 2013)

where Q is the net charge in the flux tube segment. Using the divergence theorem and that the perpendicular electric field component is zero in the center of a U-potential (see figure 1.2), (2.4) becomes

$$\oiint_S \boldsymbol{E} \cdot \boldsymbol{dS} = \frac{Q}{\epsilon} \tag{2.5}$$

$$\Rightarrow E_z(z+h,t)A(z+h) - E_z(z,t)A(z) = \frac{\rho_l(z,t)h}{\epsilon} \tag{2.6}$$

$$\Rightarrow E_z(z+h,t)\frac{SB_S}{B(z+h)} - E_z(z,t)\frac{SB_S}{B(z)} = \frac{\rho_l(z,t)h}{\epsilon} \tag{2.7}$$

where $A(z)$ is the cross section of a flux tube (see figure 2.1b), $\rho(z,t)_l$ is the charge per unit length of flux tube (in C/m) and h is the length of the flux tube segment. We now reproduce the important steps of the procedure explained more in details in Gunell et al. (2013). To get to an expression for $E(z,t)$, we can rearrange (2.7) and take the limit $h \longrightarrow 0$ such that the left-hand side of the equation becomes a derivative:

$$\frac{d}{dz}\left(\frac{B_S}{B(z)}E_z(z,t)\right) = \frac{\rho_l}{S\epsilon} \tag{2.8}$$

which we can integrate over z from the magnetospheric end of our flux tube ($z = 0$) to z:

$$\frac{B_S}{B(z)}E(z,t) - \cancelto{1}{\frac{B_S}{B_S}}E_S(t) = \frac{1}{S\epsilon}\int_0^z \rho_l(z,t)dz' \tag{2.9}$$

$$\Rightarrow E(z,t) = \frac{1}{S\epsilon}\frac{B(z)}{B_S}\int_0^z \rho_l(z,t)dz' + \frac{B(z)}{B_S}E_S(t). \tag{2.10}$$

If we impose an electrostatic potential difference between the magnetospheric and the ionospheric ends of our system, we can derive an expression for E_S depending on the boundary voltage. To find this expression we need to integrate (2.10) over z a second time:

$$V(z,t) - V_S(t) = -\frac{1}{S\epsilon}\int_0^z \frac{B(z')}{B_S}\left(\int_0^z {}'\rho_l(z,t)dz''\right)dz' - E_S(t)\int_0^z \frac{B(z')}{B_S}dz' \tag{2.11}$$

$$\Rightarrow E_S(t) = -V(z,t) + \frac{1}{S\epsilon}\int_0^z \frac{B(z')}{B_S}\left(\int_0^{z'} \rho_l(z,t)dz''\right)dz' \int_0^z \frac{B(z')}{B_S}dz' \tag{2.12}$$

where we choose a magnetospheric potential $V_S(t) = 0$. If we choose an ionospheric potential $V_i(t)$, we can express E_S as

$$E_S(t) = -\frac{V_i(t) + \frac{1}{S\epsilon}\int\limits_0^{z_i} \frac{B(z')}{B_S}\left(\int\limits_0^{z''} \rho_l(z,t)dz''\right)dz'}{\int\limits_0^{z_i} \frac{B(z')}{B_S}dz'}. \tag{2.13}$$

Observe that S, B_S and $B(z)$ are known properties of the system, and that we choose the ionospheric potential V_i. Furthermore, ρ_l can be expressed as a function of the distribution function:

$$\rho_l(z,t) = \sum_k q_k \int f_k(z, v_z, \mu, t) dv_z d\mu \tag{2.14}$$

where q_k is the electric charge of the k-th species. This means that by replacing the expression for $E_S(t)$ found in (2.13) into the expression for $E(z,t)$ found in (2.10), and by replacing the electric field in the Vlasov equation (2.2), we obtain one equation for each species describing the evolution of the distribution function over space and time that is ready to be solved numerically. To implement it, Gunell et al. (2013) use a leap-frog scheme described more in detail in the paper by Filbet et al. (2001).

We made the approximation earlier of placing ourselves in the center of the arc to be able to consider only the parallel electric field component. For positions off center where the perpendicular electric field is non zero and the plasma might drift along the arc, we can use a frame of reference moving with the plasma drift velocity. In that frame of reference we are back with a plasma that moves only along the magnetic field line and a zero perpendicular electrical field, which makes all the equations above still valid (see Gunell et al., 2013 for more details).

2.2 Important parameters

In this section, the physical parameters important to the stability and behaviour of the simulation are described. These are the boundary densities, the magnetic field configuration, and the dielectric constant.

2.2.1 Densities at the boundaries

An important parameter influencing the stability of double layers is the density of the ions and electrons at the boundaries. In the case of strong double layers, i.e. where the potential drop is much larger than the voltage equivalent of the thermal energies of both the electrons and ions, Langmuir (1929) showed that the electron and ion currents through the double layer need to be balanced, such that

$$\frac{j_e}{j_i} = \sqrt{\frac{m_i}{m_e}} \tag{2.15}$$

where $j_e = q_e n_e v_e$ and $j_i = q_i n_i v_i$. The ions are typically flowing from the high potential side to the low potential side, and electrons flow in the opposite direction. In the case of strong double layers, the thermal energy of the particles is not sufficient to cross the double layer in the other direction. For upward current regions typically associated with auroral arcs, the high potential side is on the ionospheric side, and electrons flow downward through the double layer towards the ionosphere while ions flow upward towards the magnetotail. Hence, important parameters influencing the stability and the position of the double layer are the temperatures and the densities of both the magnetospheric electrons and the ionospheric ions. For example, if the density of the ionospheric ions would come to increase at the ionospheric boundary, the double layer would move further away from the ionosphere, as the position where the flows are balanced shifts upward.

2.2.2 Magnetic field configuration

Another important factor for the stability of double layers is the configuration of the magnetic field. The Langmuir condition (2.15) has been verified in laboratory experiments with uniform magnetic field configurations. However, for converging magnetic field configurations, laboratory experiments show that the stability position of the double layer moves toward the converging magnetic field (e.g. Sato et al., 1986). Song et al. (1992) explain that the magnetic mirroring configuration modifies the shape of the magnetic flux tube. If the magnetic field B_i at the ionospheric end gets stronger, it reduces the cross-section of the magnetic flux tube at the ionospheric end, which will reduce the total flux-density of ionospheric particles at higher altitudes. As the flow of ionospheric particles through the double layer is reduced, the equilibrium position of the double layer moves closer to the ionosphere.

For our experiment, we use the same magnetic model as in Gunell et al. (2013), which approximates the $L = 7$ shell. We change the length of the magnetic flux tube which is reduced from 5.5×10^7 m to 5.2×10^7 m. We also change the magnetic flux density at the ionospheric end of the system to make it match the magnetic field conditions at 400km of altitude over Tromsø, modeled with the 11-th generation of the International Geomagnetic Reference Field (IGRF).

2.2.3 Dielectric constant

To properly study the evolution of structures due do the dynamic plasma behavior, we need to solve the Vlasov equation (2.2) with space and time steps on the characteristic spatial and time scales of the plasma, defined by the Debye length and the plasma frequency:

$$\lambda_D = \sqrt{\frac{\epsilon_0 k_B T_e}{|q|n}} \qquad ; \qquad \omega_p = \sqrt{\frac{ne^2}{m\epsilon_0}}. \tag{2.16}$$

Doing this for each species over the whole length of the magnetic flux tube and for several minutes would require immense computational power. A tweak used by Gunell et al. (2013) is to introduce an artificial relative dielectric constant ϵ_r. This changes the total dielectric constant $\epsilon = \epsilon_0 \epsilon_r$, which in turn modifies the Debye length and the plasma frequency by a factor $\sqrt{\epsilon_r}$:

$$\lambda_D' = \lambda_D \sqrt{\epsilon_r} \qquad ; \qquad \omega_p' = \omega_p \frac{1}{\sqrt{\epsilon_r}}. \tag{2.17}$$

This artificial relative dielectric constant is defined as

$$\epsilon_r = \max\left(1, (a\omega_p \Delta t)^2\right) \tag{2.18}$$

where a is a constant of choice and Δt is the size of the time steps. Defining it as such gives the new plasma period

$$T_p' = \frac{2\pi}{\omega_p'} = \frac{2\pi}{\omega_p \frac{1}{\sqrt{\epsilon_r}}} = \frac{2\pi}{\frac{\cancel{\omega_p}}{a\cancel{\omega_p}\Delta t}} = 2\pi a \Delta t. \tag{2.19}$$

Hence, our time step Δt will always be $2\pi a$ times smaller than the plasma period. Using this method for reducing the plasma period and increasing the Debye length allows us to solve the Vlasov equation over a coarser space-time grid while still being able to observe structures or physical processes normally happening on a much smaller space and/or time scale. The size of double layers will for example increase by a factor $\sim \sqrt{\epsilon_r}$. However, one should be careful when changing the physical dielectric constant: it is important for the new scales of the structures of interest to still be smaller than the typical scales over which the plasma properties are changing. Otherwise, the structures might not appear or, if they appear, behave in an non-physical way.

The technique used by Gunell et al. (2013; 2015b; 2015a) and also in the simulations presented in section 5 of this thesis is to start with a high value of ϵ_r over which the system can be run for several minutes to have time to fill up with particles from the magnetospheric and ionospheric boundaries. Then, ϵ_r can be decreased and the system run for a few minutes with this new ϵ_r, preferably until a steady state is reached. The procedure can then be repeated several times until the space and/or time scales of the physical processes we are interested in become smaller than the scales of the changes in plasma properties. That way, the system converges towards a realistic solution while saving computing power and time.

/3

Ionospheric electron-transport model

In the upper atmosphere, energetic electrons streaming down along the magnetic field are colliding with neutrals, causing ionizations and auroral emissions. It is therefore of interest for better understanding the auroral activity to study the transport of these electrons. For this purpose, several simulation models have been developed.

We can classify the different ionospheric electron-transport models in roughly three categories (Solomon, 2001; Gustavsson, 2022, accepted for publication in JGR), even though some hybrid models might exist (e.g. Solomon, 2001): the continuous energy-deposition methods, the Monte Carlo methods, and the multi-stream methods. Continuous energy-deposition methods use laboratory measurements of different interactions between a beam of electrons and matter, and rescale them to make altitude profiles of the ionospheric response. They are of good accuracy, but are not suitable for time-dependent calculations. Monte Carlo methods (e.g. Solomon, 1993; Solomon, 2001) follow the propagation of individual electrons and compute their interactions, electron by electron. They are extremely accurate in the sense that they model the discreteness of electron-collisions, but the number of electrons that can be modelled is limited by computational power. As each individual electron-path is the outcome of a number of random collisions, the limitation in the number of electrons possible to trace can lead to counting-statistics uncertainty. Things get even worse if one wants to make a time-dependent model, as each individual electrons will also have to be followed through time. Multi-stream methods (e.g. Lummerzheim and Lilensten, 1994; Peticolas and Lummerzheim, 2000; Gustavsson, 2022, accepted for publication in JGR) solve the Boltzmann equation by discretizing the energy, angular and spatial dimensions and calculate the redistribution of electrons between those bins due to collisions. They are quite powerful, as they allow modelling a large number of electrons while keeping computational time reasonable. Furthermore, time-dependent calculations can be achieved by discretizing also the time dimension, and this with reasonable increase in computational time.

Peticolas and Lummerzheim (2000) were the first to solve the time-dependent transport equation, but with a price of approximations, primarily considering only field aligned precipitation of primary electrons, ignoring their pitch-angle scattering, and ignoring the transport of secondary electrons with energies below 100 eV. This model is not possible to use in our work as it does not calculate the upward electron fluxes escaping out of the ionosphere, with no back-scattering of the primary electrons nor upward transport of the secondary electrons. Thanks to improvement in computational power over the last 20 years, Gustavsson (2022, accepted for publication in JGR) was able to make a multi-stream model solving the time-dependent transport equation which properly models the scattering and transport of all energetic electrons, primary as well as secondary. It is this model we have improved and modified to be used in this project.

In section 3.1, we explain how the following time-dependent electron-transport equation can be derived from the Boltzmann equation:

$$\begin{aligned}\frac{1}{v(E)}\frac{\partial I(s,\mu,E,t)}{\partial t}+\mu\frac{\partial I(s,\mu,E,t)}{\partial s} =& -AI(s,\mu,E,t)\\ &+B(s,\mu,E,t,I)\\ &+Q(s,\mu,E,t,I)\\ &+n_e\frac{\partial L_{ee}(E)I(s,\mu,E,t)}{\partial E}.\end{aligned} \tag{3.1}$$

In section 3.2, we describe how this transport equation is implemented numerically.

3.1 Transport equation

To model our time dependent transport of energetic electrons in the ionosphere, we start by taking the Boltzmann equation describing the spatio-temporal

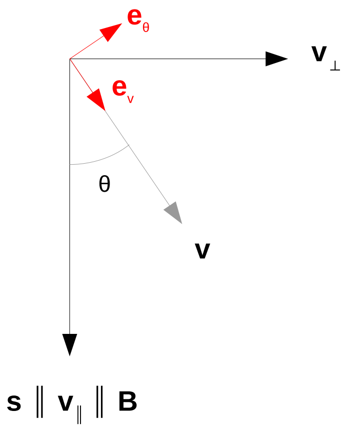

Figure 3.1: Relations between our coordinate systems $(v_{\|}, v_{perp})$ and (v, θ).

evolution of the distribution function $f(\boldsymbol{r}, \mathbf{v}, t)$:

$$\frac{Df(\boldsymbol{r}, \mathbf{v}, t)}{Dt} = \left(\frac{\partial f(\boldsymbol{r}, \mathbf{v}, t)}{\partial t}\right)_{coll}. \tag{3.2}$$

We are here interested in the field aligned motion of electrons, as the transport of electrons perpendicular to the magnetic field is negligible compared to parallel transport. This is true as long as the gyro-frequency of the electrons is larger than the collision frequency, which is the case in the upper atmosphere. Hence, we have only one spatial dimension, s, the distance along the magnetic field line. We have two velocity dimensions for which we can use two different coordinate systems, $(v_{\|}, v_{perp})$ or (v, θ) (see figure 3.1).

By replacing $\boldsymbol{r}$ with our new coordinate and developing the total derivative in time for our distribution function $f(s, \mathbf{v}, t)$, we get:

$$\frac{\partial f}{\partial t} + \frac{\partial f}{\partial s}\frac{ds}{dt} + \frac{\partial f}{\partial \mathbf{v}} \cdot \frac{d\mathbf{v}}{dt} = \left(\frac{\partial f}{\partial t}\right)_{coll}. \tag{3.3}$$

The total derivative in the second term on the left-hand side can be rewritten as

$$\frac{ds}{dt}\frac{\partial f}{\partial s} = v_{\|}\frac{\partial f}{\partial s} = \mu v \frac{\partial f}{\partial s} \tag{3.4}$$

where μ is here defined as the cosine of the pitch-angle θ, $\mu = cos(\theta)$. It is not to confuse with the magnetic moment that was also designated with the symbol μ in chapter 2. We keep the notation μ for the cosine of the pitch-angle here as it is the symbol commonly used in the ionospheric physics literature. In the third term on the left-hand side in (3.3), the term $\partial f/\partial \mathbf{v}$ is a gradient in velocity space, which in our polar coordinate system $(v,\ \theta)$ becomes

$$\frac{\partial f}{\partial \mathbf{v}} = \boldsymbol{\nabla}_{\mathbf{v}} f = \frac{\partial f}{\partial v}\mathbf{e}_v + \frac{1}{v}\frac{\partial f}{\partial \theta}\mathbf{e}_\theta. \tag{3.5}$$

To develop $d\mathbf{v}/dt$, we first express it in the coordinate system $(v_{\|}, v_{\perp})$:

$$\frac{d\mathbf{v}}{dt} = \frac{dv_{\|}}{dt}\mathbf{e}_{\|} + \frac{dv_{\perp}}{dt}\mathbf{e}_{\perp}. \tag{3.6}$$

We then use the following transformation of coordinate system (see figure 3.1):

$$\begin{cases} \mathbf{e}_{\|} = cos(\theta)\mathbf{e}_v - sin(\theta)\mathbf{e}_\theta \\ \mathbf{e}_{\perp} = sin(\theta)\mathbf{e}_v + cos(\theta)\mathbf{e}_\theta \end{cases} \tag{3.7}$$

which once replaced in equation (3.6) gives us

$$\begin{aligned} \frac{d\mathbf{v}}{dt} = &\left(\frac{dv_{\|}}{dt}cos(\theta) + \frac{dv_{\perp}}{dt}sin(\theta)\right)\mathbf{e}_v \\ &+ \left(-\frac{dv_{\|}}{dt}sin(\theta) + \frac{dv_{\perp}}{dt}cos(\theta)\right)\mathbf{e}_\theta. \end{aligned} \tag{3.8}$$

We can then use Newton's second law to express $dv_{\|}/dt$ and $dv_{\perp}/dt$. The forces applied on the system are the gravitation force, the electric force and the magnetic mirroring force. However, we can consider the effects of the gravitation force as negligible on these scales compared with the other forces. We get for the component parallel to the magnetic field

$$\frac{dv_{\|}}{dt} = \frac{qE_{\|}}{m} - \frac{v_{\perp}^2}{2B}\frac{dB}{ds}. \tag{3.9}$$

Considering only the electric field component parallel to B, the only force working on the component perpendicular to the magnetic field is the mirroring force. The mirroring configuration is going to make the perpendicular velocity of a particle increase as the particle moves into a stronger magnetic field. Mathematically, we can derive this effect from the invariance of the magnetic moment:

$$\frac{d}{dt}\left(\frac{mv_{\perp}^2}{2B}\right) = 0 \tag{3.10}$$

$$\Rightarrow \quad \frac{\frac{d}{dt}(mv_{\perp}^2)2B - mv_{\perp}^2\frac{dB}{dt}}{4B^2} = 0 \tag{3.11}$$

$$\Rightarrow \quad \frac{d}{dt}(v_{\perp}^2) = \frac{v_{\perp}^2}{2B}\frac{dB}{dt}. \tag{3.12}$$

It could be tempting to cancel the right-hand side of equation (3.12) as the magnetic field does not vary with time but only through space. However, as the particle moves along the spatial dimension s, the effective magnetic field that is perceived by the particle changes. We can use the chain rule:

$$\frac{dB(s)}{dt} = \frac{dB}{ds}\frac{ds}{dt} = \frac{dB}{ds}\mu v \tag{3.13}$$

which replaced in equation (3.10) gives us

$$\frac{d}{dt}(v_\perp^2) = \frac{v_\perp^2}{2B}\frac{dB}{ds}\mu v \tag{3.14}$$

$$\Rightarrow \quad 2v_\perp \frac{dv_\perp^2}{dt} = \mu v \frac{v_\perp^2}{2B}\frac{dB}{ds} \tag{3.15}$$

$$\Rightarrow \quad \frac{dv_\perp}{dt} = \mu v \frac{v_\perp}{4B}\frac{dB}{ds}. \tag{3.16}$$

We have now found an expression for $dv_\parallel$ in (3.9) and an expression for $dv_\perp$ in (3.16). Inserting these in (3.8), we get

$$\begin{aligned}\frac{d\mathbf{v}}{dt} &= \left(\frac{qE_\parallel}{m}cos(\theta) - \frac{v_\perp^2}{4B}\frac{dB}{ds}cos(\theta) + \mu v\frac{v_\perp}{4B}\frac{dB}{ds}sin(\theta)\right)\mathbf{e}_v \\ &\quad + \left(-\frac{qE_\parallel}{m}sin(\theta) + \frac{v_\perp^2}{2B}\frac{dB}{ds}sin(\theta) + \mu v\frac{v_\perp}{4B}\frac{dB}{ds}cos(\theta)\right)\mathbf{e}_\theta \\ &= \left(\frac{qE_\parallel}{m}cos(\theta) - cos(\theta)sin^2(\theta)\frac{v^2}{4B}\frac{dB}{ds} + cos(\theta)sin^2(\theta)\frac{v^2}{4B}\frac{dB}{ds}\right)\mathbf{e}_v \\ &\quad + \left(-\frac{qE_\parallel}{m}sin(\theta) + sin^2(\theta)sin(\theta)\frac{v^2}{4B}\frac{dB}{ds} + cos^2(\theta)sin(\theta)\frac{v^2}{4B}\frac{dB}{ds}\right)\mathbf{e}_\theta \\ &= \left(\frac{qE_\parallel}{m}\mu\right)\mathbf{e}_v + \left(-\frac{qE_\parallel}{m} + \frac{v^2}{2B}\frac{dB}{ds}\right)sin(\theta)\mathbf{e}_\theta \end{aligned} \tag{3.17}$$

where we have used that $\mu = cos(\theta)$ and that $v_\perp = vsin(\theta)$ (see figure 3.1). By using the expression for $d\mathbf{v}/dt$ found in (3.17) and the expression for $\partial f/\partial \mathbf{v}$ found in (3.5) we get for the third element of the left-hand side in (3.3):

$$\begin{aligned}\frac{d\mathbf{v}}{dt}\cdot\frac{\partial f}{\partial \mathbf{v}} &= \frac{qE_\parallel}{m}\mu\frac{\partial f}{\partial v} + \left(-\frac{qE_\parallel}{m} + \frac{v^2}{2B}\frac{dB}{ds}\right)\frac{sin(\theta)}{v}\frac{\partial f}{\partial \theta} \\ &= \frac{qE_\parallel}{m}\mu\frac{\partial f}{\partial v} - \left(\frac{qE_\parallel}{m} - \frac{v^2}{2B}\frac{dB}{ds}\right)\frac{sin^2(\theta)}{v}\frac{\partial f}{\partial sin(\theta)\theta} \\ &= \frac{qE_\parallel}{m}\mu\frac{\partial f}{\partial v} + \left(\frac{qE_\parallel}{m} - \frac{v^2}{2B}\frac{dB}{ds}\right)\frac{1-\mu^2}{v}\frac{\partial f}{\partial \mu} \end{aligned} \tag{3.18}$$

where we used that $d\mu = -sin(\theta)d\theta$. Replacing in equation (3.3), we have

$$\frac{\partial f}{\partial t} + \mu v\frac{\partial f}{\partial s} + \frac{q}{m}E_\parallel\mu\frac{\partial f}{\partial v} + \left(\frac{q}{m}E_\parallel - \frac{v^2}{2B}\frac{dB}{ds}\right)\frac{1-\mu^2}{v}\frac{\partial f}{\partial \mu} = \left(\frac{\partial f}{\partial t}\right)_{coll}. \tag{3.19}$$

From this equation, we can see that the only force changing the total velocity (i.e. kinetic energy) of particles is due to parallel electric fields. The magnetic mirroring configuration does not change the energy as any increase or decrease in perpendicular velocity will be compensated by an opposite change in parallel velocity. It changes, however, the pitch-angle. Pitch-angle that is also affected by parallel electric fields.

Note that the 1-D Boltzmann equation (3.19) is found in the literature, but often presented without any explanation (e.g. Schunk and Nagy, 2009) or sometimes referencing old reviews from the 60s that are challenging to trace (e.g. Khazanov et al. (1994) referencing to Sivukhin (1965)). It is for this reason we decided to present a full derivation here.

There seems however to be another way to derive this equation found in the thesis by Guio (1998), where the change of the cosine of the pitch-angle μ due to the magnetic mirroring configuration depends only on the position along the magnetic field line. The term $\frac{\partial f}{\partial \mu}\frac{d\mu}{dt}$ can then be considered a spatial dimension, and the cosine of the pitch-angle μ written as a function of s, so that $\frac{d\mu}{dt} = \frac{\partial \mu}{\partial s}\frac{ds}{dt}$, where ds/dt can be derived utilizing that the magnetic moment is a constant of motion. To obtain the same Boltzmann equation as (3.19), one could follow the derivations done earlier in this thesis for $d\mathbf{v}/dt$, but by considering μ a velocity dimension again to account for the parallel electric fields effects, and omitting the mirror force. Both methods lead then to the same result, but the method presented here feels more transparent and perhaps also more elegant.

Turning back to our Boltzmann equation (3.19), we consider a further approximation: even though parallel electric fields and the converging magnetic field configuration have an important effect on the acceleration of electrons in the magnetosphere (see chapter 1), their effects on electron-transport in the ionosphere are negligible as collision frequencies become important (Peticolas and Lummerzheim, 2000). This means that all $qE_{\|}/m$ and dB/ds terms vanish:

$$\frac{\partial f(s,\mu,v,t)}{\partial t} + \mu v \frac{\partial f(s,\mu,v,t)}{\partial s} = \left(\frac{\partial f(s,\mu,v,t)}{\partial t}\right)_{coll}. \qquad (3.20)$$

Then, we note that it is possible to replace our velocity coordinate v by an energy coordinate E using that $E = \frac{1}{2}mv^2$:

$$\frac{\partial f(s,\mu,E,t)}{\partial t} + \mu v(E) \frac{\partial f(s,\mu,E,t)}{\partial s} = \left(\frac{\partial f(s,\mu,E,t)}{\partial t}\right)_{coll}. \qquad (3.21)$$

We can now transform this Boltzmann equation for the electron distribution function f into a transport equation for the electron flux I using that $I = vf$:

$$\frac{1}{v(E)}\frac{\partial I(s,\mu,E,t)}{\partial t} + \mu \frac{\partial I(s,\mu,E,t)}{\partial s} = \left(\frac{\partial I(s,\mu,E,t)}{\partial t}\right)_{coll}. \qquad (3.22)$$

The last step is then to express the right-hand side of equation (3.22) which corresponds to the sources and losses of electron flux due to collisions. Following the AURORA code documentation:

$$\begin{aligned}\frac{1}{v(E)}\frac{\partial I(s,\mu,E,t)}{\partial t}+\mu\frac{\partial I(s,\mu,E,t)}{\partial s} =& -AI(s,\mu,E,t) \\ &+B(s,\mu,E,t,I) \\ &+Q(s,\mu,E,t,I) \\ &+n_e\frac{\partial L_{ee}(E)I(s,\mu,E,t)}{\partial E}\end{aligned} \tag{3.23}$$

The first term on the right-hand side represents all the losses of electron flux from energy E and pitch-angle μ. These losses are due to both elastic collisions changing only μ and inelastic collisions changing both E and μ:

$$A=\sum_k n_k(s)\sigma_k^{tot}(E) \tag{3.24}$$

where $\sigma_k^{tot}(E)$ is the total cross-section for collision of electrons at energy E with atoms of the k-th species.

The second term on the right-hand side represents the elastic collisions scattering electron fluxes from other pitch-angle μ' to the pitch-angle μ, without changing the energy:

$$B=\sum_k n_k(s)\sigma_k^{elastic}(E)\int_{-1}^{1} p_k^{elastic}(E,\mu'\longrightarrow\mu)I(s,\mu',E,t)d\mu' \tag{3.25}$$

where $p_k^{elastic}(E,\mu'\longrightarrow\mu)$ is the probability for an electron with pitch-angle μ' to scatter to pitch-angle μ for elastic collisions with species k.

The third term on the right-hand side represents both the inelastic collisions and ionization collisions scattering electron fluxes from other pitch-angle μ' and energy E' to pitch-angle μ and energy E:

$$\begin{aligned}&Q(E,s,\mu,t,I)=Q_{local}(s,\mu,E,t) \\ &+\sum_k n_k(s)\sigma_k^{j,inel}\underset{j}{(E'\to E)}\int_{-1}^{1} p_k^{j,inel}(E',\mu'\to\mu)I(s,\mu',E',t)d\mu'dE' \\ &+\sum_k n_k(s)\int_{E+E^*}^{\infty}\sigma_k^{j,ion}(E'\to E)\int_{-1}^{1} p_k^{j,ion}(E',\mu'\to\mu)I(s,\mu',E',t)d\mu'dE'\end{aligned} \tag{3.26}$$

where the first term on the right-hand side represents the source of photoelectrons and secondary electrons created by ionization collisions. The summations in the second and third term on the right-hand side are over all excited states j of the k-th species. The abbreviations *inel* and *ion* stand for inelastic collisions and ionization collisions respectively. The term E* appearing in the third term represents the minimum ionization energy for an atom or molecule of species k.

The fourth and last term on the right-hand side of (3.23) represents the losses of electron fluxes due to energy transfer to ambient thermal ionospheric electrons.

3.2 Numerical implementation

Now with the time-dependent electron-transport equation (3.23) properly derived, we turn to a description of the numerical implementation. The full code of the model can be found at https://github.com/egavazzi/AURORA.

3.2.1 Energy discretization

In the ionosphere, energetic electrons undergo only energy degradation. This means that the electron-transport equation (3.23) for electrons with energy E_i does not depend on electron fluxes at lower energies. The equation can thus be solved over time, space and pitch-angle, in a loop towards lower energies. We start with the highest energy E_{max}, for which $Q = 0$, and then use the flux $I(s, \mu, E_{max}, t)$ obtained to calculate $Q(s, \mu, E, t)$ for all the lower energies E. Then, every time we compute the flux for an energy, we update $Q(s, \mu, E, t)$ for all lower energies, until we reach the lowest energy of our energy grid. This discretization in energy allows us to rewrite the last term of the right-hand side of equation (3.23) as follow (Gronoff et al., 2012):

$$\begin{aligned} n_e \frac{\partial L_{ee}(E) I(s,\mu,E,t)}{\partial E} &= \frac{1}{v(E_{i+1})} \frac{\partial \epsilon_{ee_{i+1}}}{\partial t} \frac{I(s,\mu,E_{i+1},t)}{\Delta E_{i+1}} \\ &\quad - \frac{1}{v(E_i)} \frac{\partial \epsilon_{ee_i}}{\partial t} \frac{I(s,\mu,E_i,t)}{\Delta E_i} \end{aligned} \tag{3.27}$$

where $\frac{\partial \epsilon_{ee}}{\partial t}$ is the electron energy-loss rate (Swartz et al., 1971):

$$\frac{\partial \epsilon_{ee_i}}{\partial t} = \frac{3.0271 \cdot 10^{-10} n_e^{0.97}}{E_i^{0.44}} \left(\frac{E_i - E_e}{E_i - 0.53 E_e} \right)^{2.36} \qquad (eV/s) \tag{3.28}$$

where E_e is the electron thermal energy in eV. The first term is a source of electron flux from the next higher energy bin and thus can be merged into Q. The second term is a loss of electron flux and can be merged into A. Note also that as we discretize in energy, a fraction of the electrons in an energy bin that collide inelastically might remain in the energy bin instead of cascading to the lower ones. The fraction staying in the energy bin between E_i and E_{i+1} is

$$\max\left(0, 1 - \frac{\Delta E_k^j}{E_{i+1} - E_i}\right) \tag{3.29}$$

where ΔE_k^j is the energy lost in the collision with an atom or molecule of the k-th species in its j-th excited state. To account for this effect, we modify B and Q using this factor so that the fraction of electron flux staying in the energy bin is effectively counted as elastic collisions instead of inelastic.

3.2.2 Pitch-angle discretization

Furthermore, we can divide the electron flux in discrete pitch-angle streams, with μ_l the cosine of the pitch-angle θ from -1 to 1. This transforms equation (3.23) into a system of equations, with one equation for each discrete stream μ_l:

$$\begin{aligned}\frac{1}{v(E_i)}\frac{\partial I^{\mu_l}(s,E_i,t)}{\partial t} + \bar{\mu}_l\frac{\partial I^{\mu_l}(s,E_i,t)}{\partial s} = &- A' I^{\mu_l}(s,E_i,t)\\ &+ \sum_{\mu_k} B'(s,\mu_k \longrightarrow \mu_l, E_i) I^{\mu_k}(s,E_i,t)\\ &+ Q'(s,\mu_l,E_i,t)\end{aligned} \tag{3.30}$$

where μ_k indicates the other pitch-angle streams, and $\bar{\mu}_l$ is the average of the pitch-angle cosine in stream l as the distribution of electrons in each stream is considered isotropic. For n streams, the system of equations to solve inside the energy loop over time and space becomes (from AURORA documentation):

$$\frac{1}{v}\frac{\partial}{\partial t}\begin{pmatrix} I^1 \\ I^2 \\ \vdots \\ I^n \end{pmatrix} + \frac{\partial}{\partial s}\begin{pmatrix} \bar{\mu}_1 I^1 \\ \bar{\mu}_2 I^2 \\ \vdots \\ \bar{\mu}_n I^n \end{pmatrix} = \begin{pmatrix} -A' + B'_{11} & B'_{21} & \cdots & B'_{n1} \\ B'_{12} & -A' + B'_{21} & \cdots & B'_{n2} \\ \vdots & \vdots & \ddots & \vdots \\ B'_{1n} & B'_{2n} & \cdots & -A' + B'_{nn} \end{pmatrix}\begin{pmatrix} I^1 \\ I^2 \\ \vdots \\ I^n \end{pmatrix} + \begin{pmatrix} Q^1 \\ Q^2 \\ \vdots \\ Q^n \end{pmatrix} \tag{3.31}$$

where each I^l and Q^l are arrays of size (n_z x 1), and A and B_{kl} are diagonal matrices of size (n_z x n_z). The matrix on the right-hand side has then a size ($n_z n_\mu$ x $n_z n_\mu$).

3.2.3 Crank-Nicolson scheme

To solve the linear system of equation (3.31) over time and space, we use a Crank Nicolson scheme with backward differences in space. A Crank-Nicolson scheme uses a combination of forward and backward differences in time to obtain a numerically stable implicit scheme with a quite good accuracy. To make the following explanations easier to follow, we use only two streams, an upward electron-stream ${}^U I$ and a downward electron-stream ${}^D I$. In a grid with n nodes in time and i nodes in space, starting with the upward electron-stream,

Forward in time, backward in space:

$$\frac{1}{v}\frac{\left({}^U I_i^{n+1} - {}^U I_i^n\right)}{\Delta t} + \bar{\mu}_U \frac{\left({}^U I_i^n - {}^U I_{i-1}^n\right)}{\Delta s} = -A'\left({}^U I_i^n\right) + B'\left({}^D I_i^n\right) + {}^U Q_i'^n \tag{3.32}$$

Backward in time, backward in space:

$$\frac{1}{v}\frac{\left({}^U I_i^{n} - {}^U I_i^{n-1}\right)}{\Delta t} + \bar{\mu}_U \frac{\left({}^U I_i^n - {}^U I_{i-1}^n\right)}{\Delta s} = -A'\left({}^U I_i^n\right) + B'\left({}^D I_i^n\right) + {}^U Q_i'^n \tag{3.33}$$

where $i = 1$ corresponds to the bottom of the ionosphere and $i = end$ to the top of the ionosphere, as the stream of electron is moving upward (see figure 3.2).

By using backward in time for the node n+1 instead of the node n, we get

Backward in time, backward in space:

$$\frac{1}{v}\frac{\left({}^U I_i^{n+1} - {}^U I_i^n\right)}{\Delta t} + \bar{\mu}_U \frac{\left({}^U I_i^{n+1} - {}^U I_{i-1}^{n+1}\right)}{\Delta s} = -A'\left({}^U I_i^{n+1}\right) + B'\left({}^D I_i^{n+1}\right) + {}^U Q_i'^{n+1}. \tag{3.34}$$

By adding equations (3.32) + (3.34), we obtain the Crank-Nicolson scheme for the upward electron-stream:

$$\begin{aligned} \frac{1}{v}\frac{\left({}^U I_i^{n+1} - {}^U I_i^n\right)}{\Delta t} + \bar{\mu}_U \frac{\left({}^U I_i^{n+1} - {}^U I_{i-1}^{n+1} + {}^U I_i^n - {}^U I_{i-1}^n\right)}{2\Delta s} &= \\ -\frac{A'}{2}\left({}^U I_i^{n+1} + {}^U I_i^n\right) + \frac{B'}{2}\left({}^D I_i^{n+1} + {}^D I_i^n\right) + {}^U Q_{average} & \end{aligned} \tag{3.35}$$

with ${}^U Q_{average} = \frac{1}{2}\left({}^U Q_i'^{n+1} + {}^U Q_i'^n\right)$. By separating the $n+1$ and n terms on each side, we get

$$\begin{aligned} \left(Ddt - DdZu + \frac{A'}{2}\right) {}^U I_i^{n+1} + DdZu\, {}^U I_{i-1}^{n+1} - \frac{B'}{2}\, {}^D I_i^{n+1} &= \\ \left(Ddt + DdZu - \frac{A'}{2}\right) {}^U I_i^{n} - DdZu\, {}^U I_{i-1}^{n} + \frac{B'}{2}\, {}^D I_i^{n} + {}^U Q_{average} & \end{aligned} \tag{3.36}$$

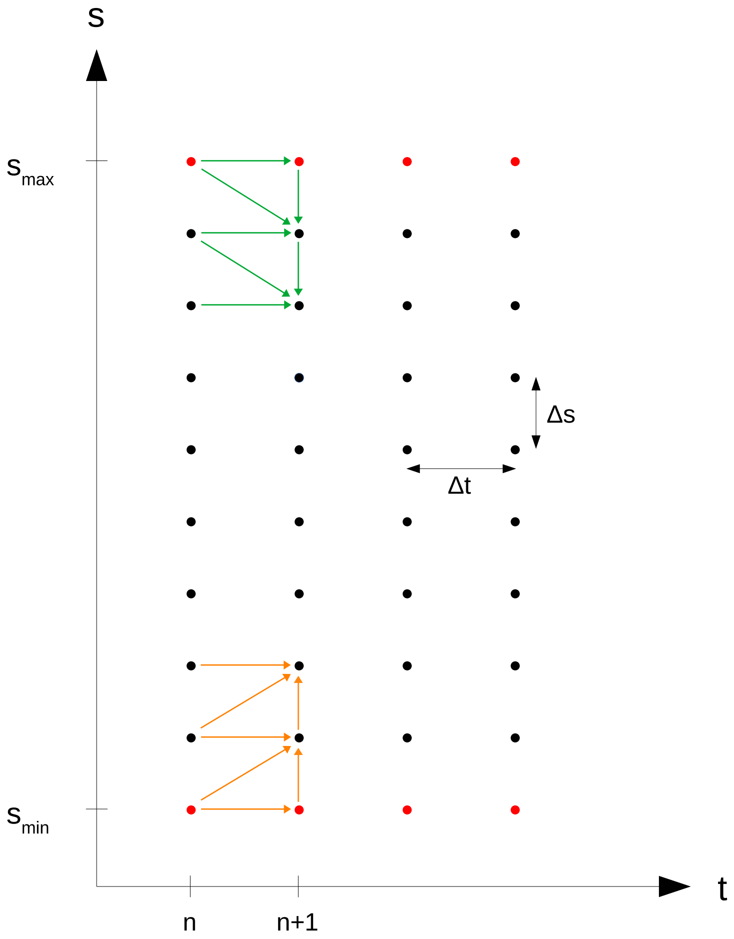

Figure 3.2: Stencil of our Crank-Nicolson scheme. The red nodes are the boundaries of our ionosphere, the orange arrows represent the scheme for the up-going streams of electrons and the green arrows represent the scheme for the down-going streams. It is clear from the stencil that $i = 1$ and $i = end$ are not going to be the same for the up-going streams and the down-going streams.

where $Ddt = \frac{1}{v\Delta t}$ and $DdZu = \frac{\bar{\mu}_U}{2\Delta s}$.

For the downward electron-stream, using the same method, we get

$$\begin{aligned} &\left(Ddt + DdZd + \frac{A'}{2}\right) {}^{D}I_i^{n+1} - DdZd^{D}I_{i-1}^{n+1} - \frac{B'}{2} {}^{U}I_i^{n+1} = \\ &\left(Ddt - DdZd - \frac{A'}{2}\right) {}^{D}I_i^{n} + DdZd^{D}I_{i-1}^{n} + \frac{B'}{2} {}^{U}I_i^{n} + {}^{D}Q_{average} \end{aligned} \tag{3.37}$$

with the difference that as the beam is propagating downward, $i = 1$ corresponds to the top of the ionosphere and $i = end$ corresponds to the bottom of the ionosphere (see figure 3.2).

We can rewrite (3.36) and (3.37) as a matrix equation:

$$\mathcal{M}\vec{I}^{n+1} = \mathcal{N}\vec{I}^{n} + \vec{Q}_{average} \tag{3.38}$$

where $\mathcal{M}$, $\mathcal{N}$, $\vec{I}^{n+1}$ and $\vec{Q}_{average}$ are as follow:

$$\mathcal{M} = \begin{bmatrix} \mathcal{M}^{\mathcal{DD}} & \mathcal{M}^{\mathcal{DU}} \\ \mathcal{M}^{\mathcal{UD}} & \mathcal{M}^{\mathcal{UU}} \end{bmatrix} \quad ; \quad \mathcal{N} = \begin{bmatrix} \mathcal{N}^{\mathcal{DD}} & \mathcal{N}^{\mathcal{DU}} \\ \mathcal{N}^{\mathcal{UD}} & \mathcal{N}^{\mathcal{UU}} \end{bmatrix}$$

$$\vec{I}^{n+1} = \begin{bmatrix} \begin{pmatrix} {}^{D}I_{end}^{n+1} \\ {}^{D}I_{end-1}^{n+1} \\ \vdots \\ {}^{D}I_{2}^{n+1} \\ {}^{D}I_{1}^{n+1} \end{pmatrix} \\ \begin{pmatrix} {}^{U}I_{1}^{n+1} \\ {}^{U}I_{2}^{n+1} \\ \vdots \\ {}^{U}I_{end-1}^{n+1} \\ {}^{U}I_{end}^{n+1} \end{pmatrix} \end{bmatrix} \quad ; \quad \vec{Q}_{average} = \frac{1}{2} \begin{bmatrix} \begin{pmatrix} {}^{D}Q'^{n+1}_{end} + {}^{D}Q'^{n}_{end} \\ {}^{D}Q'^{n+1}_{end-1} + {}^{D}Q'^{n}_{end-1} \\ \vdots \\ {}^{D}Q'^{n+1}_{2} + {}^{D}Q'^{n}_{2} \\ {}^{D}Q'^{n+1}_{1} + {}^{D}Q'^{n}_{1} \end{pmatrix} \\ \begin{pmatrix} {}^{U}Q'^{n+1}_{1} + {}^{U}Q'^{n}_{1} \\ {}^{U}Q'^{n+1}_{2} + {}^{U}Q'^{n}_{2} \\ \vdots \\ {}^{U}Q'^{n+1}_{end-1} + {}^{U}Q'^{n}_{end-1} \\ {}^{U}Q'^{n+1}_{end} + {}^{U}Q'^{n}_{end} \end{pmatrix} \end{bmatrix}$$

and the sub-matrices:

$$\mathcal{M}^{\mathcal{D}\mathcal{D}} = \begin{pmatrix} \left(\begin{smallmatrix} Ddt \\ +DdZd \\ +A'/2 \end{smallmatrix}\right) & -DdZd & 0 & \cdots & \cdots & 0 \\ 0 & \left(\begin{smallmatrix} Ddt \\ +DdZd \\ +A'/2 \end{smallmatrix}\right) & -DdZd & 0 & \cdots & 0 \\ \vdots & \ddots & \ddots & \ddots & \ddots & \vdots \\ \vdots & & \ddots & \ddots & \ddots & 0 \\ 0 & \cdots & \cdots & 0 & \left(\begin{smallmatrix} Ddt \\ +DdZd \\ +A'/2 \end{smallmatrix}\right) & -DdZd \\ 0 & \cdots & \cdots & \cdots & 0 & \left(\begin{smallmatrix} Ddt \\ +DdZd \\ +A'/2 \end{smallmatrix}\right) \end{pmatrix}$$

$$\mathcal{M}^{\mathcal{U}\mathcal{U}} = \begin{pmatrix} \left(\begin{smallmatrix} Ddt \\ -DdZu \\ +A'/2 \end{smallmatrix}\right) & 0 & \cdots & \cdots & \cdots & 0 \\ +DdZu & \left(\begin{smallmatrix} Ddt \\ -DdZu \\ +A'/2 \end{smallmatrix}\right) & 0 & \cdots & \cdots & 0 \\ 0 & \ddots & \ddots & \ddots & & \vdots \\ \vdots & \ddots & \ddots & \ddots & \ddots & \vdots \\ 0 & \cdots & 0 & +DdZu & \left(\begin{smallmatrix} Ddt \\ -DdZu \\ +A'/2 \end{smallmatrix}\right) & 0 \\ 0 & \cdots & \cdots & 0 & +DdZu & \left(\begin{smallmatrix} Ddt \\ -DdZu \\ +A'/2 \end{smallmatrix}\right) \end{pmatrix}$$

$$\mathcal{M}^{\mathcal{D}\mathcal{U}} = \mathcal{M}^{\mathcal{U}\mathcal{D}} = \begin{pmatrix} \frac{B'}{2} & 0 & \cdots & \cdots & \cdots & 0 \\ 0 & \frac{B'}{2} & 0 & \cdots & \cdots & 0 \\ \vdots & \ddots & \ddots & \ddots & & \vdots \\ \vdots & & \ddots & \ddots & \ddots & \vdots \\ 0 & \cdots & \cdots & 0 & \frac{B'}{2} & 0 \\ 0 & \cdots & \cdots & \cdots & 0 & \frac{B'}{2} \end{pmatrix}$$

$$\mathcal{N}^{\mathcal{D}\mathcal{D}} = \begin{pmatrix} \left(\begin{smallmatrix} Ddt \\ -DdZd \\ -A'/2 \end{smallmatrix}\right) & +DdZd & 0 & \cdots & \cdots & 0 \\ 0 & \left(\begin{smallmatrix} Ddt \\ -DdZd \\ -A'/2 \end{smallmatrix}\right) & +DdZd & 0 & \cdots & 0 \\ \vdots & \ddots & \ddots & \ddots & \ddots & \vdots \\ \vdots & & \ddots & \ddots & \ddots & 0 \\ 0 & \cdots & \cdots & 0 & \left(\begin{smallmatrix} Ddt \\ -DdZd \\ -A'/2 \end{smallmatrix}\right) & +DdZd \\ 0 & \cdots & \cdots & \cdots & 0 & \left(\begin{smallmatrix} Ddt \\ -DdZd \\ -A'/2 \end{smallmatrix}\right) \end{pmatrix}$$

$$\mathcal{N}^{\mathcal{UU}} = \begin{pmatrix} \left(\begin{smallmatrix} Ddt \\ +DdZu \\ -A'/2 \end{smallmatrix}\right) & 0 & \cdots & \cdots & \cdots & 0 \\ -DdZu & \left(\begin{smallmatrix} Ddt \\ +DdZu \\ -A'/2 \end{smallmatrix}\right) & 0 & \cdots & \cdots & 0 \\ 0 & \ddots & \ddots & \ddots & & \vdots \\ \vdots & \ddots & \ddots & \ddots & \ddots & \vdots \\ 0 & \cdots & 0 & -DdZu & \left(\begin{smallmatrix} Ddt \\ +DdZu \\ -A'/2 \end{smallmatrix}\right) & 0 \\ 0 & \cdots & \cdots & 0 & -DdZu & \left(\begin{smallmatrix} Ddt \\ +DdZu \\ -A'/2 \end{smallmatrix}\right) \end{pmatrix}$$

$$\mathcal{N}^{\mathcal{DU}} = \mathcal{N}^{\mathcal{UD}} = \begin{pmatrix} -\frac{B'}{2} & 0 & \cdots & \cdots & \cdots & 0 \\ 0 & -\frac{B'}{2} & 0 & \cdots & \cdots & 0 \\ \vdots & \ddots & \ddots & \ddots & & \vdots \\ \vdots & & \ddots & \ddots & \ddots & \vdots \\ 0 & \cdots & \cdots & 0 & -\frac{B'}{2} & 0 \\ 0 & \cdots & \cdots & \cdots & 0 & -\frac{B'}{2} \end{pmatrix}$$

Note that $\mathcal{M}$ and $\mathcal{N}$ are of size $(2n_z \text{ x } 2n_z)$ as we have two streams. We can multiply equation (3.38) by the inverse of $\mathcal{M}$, and we get the Crank-Nicolson updating step:

$$\vec{I}^{n+1} = \mathcal{M}^{-1}(\mathcal{N}\vec{I}^{n} + \vec{Q}_{average}) \tag{3.39}$$

which gives us the flux of electrons at any time given appropriate initial and boundary conditions. At the top of the ionosphere, we have the downward fluxes given as an input, and we use that the upward fluxes have no gradient as collision frequencies become so small that the fluxes don't change:

$$^{D}I^{n+1}_{top} = {}^{D}I^{n+1}_{input} \tag{3.40}$$

$$^{U}I^{n+1}_{top} = {}^{U}I^{n+1}_{top-1}. \tag{3.41}$$

At the bottom of the ionosphere, the upward fluxes are equal to zero as there is no upward electron flux from the lower atmosphere, and downward fluxes also tend to zero as all electrons should have scattered up or dissipated all their energy:

$$^{D}I^{n+1}_{bottom} = 0 \tag{3.42}$$

$$^{U}I^{n+1}_{bottom} = 0. \tag{3.43}$$

We modify $\mathcal{M}$, $\mathcal{N}$ and $\vec{Q}_{average}$ accordingly :

$$\mathcal{M}^{\mathcal{D}\mathcal{D}} = \begin{pmatrix} 1 & 0 & \cdots & \cdots & \cdots & 0 \\ 0 & \begin{pmatrix} Ddt \\ +DdZd \\ +A'/2 \end{pmatrix} & -DdZd & 0 & \cdots & 0 \\ \vdots & \ddots & \ddots & \ddots & \ddots & \vdots \\ \vdots & & \ddots & \ddots & \ddots & 0 \\ 0 & \cdots & \cdots & 0 & \begin{pmatrix} Ddt \\ +DdZd \\ +A'/2 \end{pmatrix} & -DdZd \\ 0 & \cdots & \cdots & \cdots & 0 & 1 \end{pmatrix}$$

$$\mathcal{M}^{\mathcal{U}\mathcal{U}} = \begin{pmatrix} 1 & 0 & \cdots & \cdots & \cdots & 0 \\ -DdZu & \begin{pmatrix} Ddt \\ +DdZu \\ +A'/2 \end{pmatrix} & 0 & \cdots & \cdots & 0 \\ 0 & \ddots & \ddots & \ddots & & \vdots \\ \vdots & \ddots & \ddots & \ddots & \ddots & \vdots \\ 0 & \cdots & 0 & -DdZu & \begin{pmatrix} Ddt \\ +DdZu \\ +A'/2 \end{pmatrix} & 0 \\ 0 & \cdots & \cdots & 0 & -1 & 1 \end{pmatrix}$$

$$\mathcal{M}^{\mathcal{D}\mathcal{U}} = \mathcal{M}^{\mathcal{U}\mathcal{D}} = \begin{pmatrix} 0 & 0 & \cdots & \cdots & \cdots & 0 \\ 0 & \frac{B'}{2} & 0 & \cdots & \cdots & 0 \\ \vdots & \ddots & \ddots & \ddots & & \vdots \\ \vdots & & \ddots & \ddots & \ddots & \vdots \\ 0 & \cdots & \cdots & 0 & \frac{B'}{2} & 0 \\ 0 & \cdots & \cdots & \cdots & 0 & 0 \end{pmatrix}$$

$$\mathcal{N}^{\mathcal{D}\mathcal{D}} = \begin{pmatrix} 0 & 0 & 0 & \cdots & \cdots & 0 \\ 0 & \begin{pmatrix} Ddt \\ -DdZd \\ -A'/2 \end{pmatrix} & +DdZd & 0 & \cdots & 0 \\ \vdots & \ddots & \ddots & \ddots & \ddots & \vdots \\ \vdots & & \ddots & \ddots & \ddots & 0 \\ 0 & \cdots & \cdots & 0 & \begin{pmatrix} Ddt \\ -DdZd \\ -A'/2 \end{pmatrix} & +DdZd \\ 0 & \cdots & \cdots & \cdots & 0 & 0 \end{pmatrix}$$

$$\mathcal{N}^{\mathcal{U}\mathcal{U}} = \begin{pmatrix} 0 & 0 & \cdots & \cdots & \cdots & 0 \\ +DdZu & \begin{pmatrix} Ddt \\ -DdZu \\ -A'/2 \end{pmatrix} & 0 & \cdots & \cdots & 0 \\ 0 & \ddots & \ddots & \ddots & & \vdots \\ \vdots & \ddots & \ddots & \ddots & \ddots & \vdots \\ 0 & \cdots & 0 & +DdZu & \begin{pmatrix} Ddt \\ -DdZu \\ -A'/2 \end{pmatrix} & 0 \\ 0 & \cdots & \cdots & \cdots & 0 & 0 \end{pmatrix}$$

$$\mathcal{N}^{\mathcal{D}\mathcal{U}} = \mathcal{N}^{\mathcal{U}\mathcal{D}} = \begin{pmatrix} 0 & 0 & \cdots & \cdots & \cdots & 0 \\ 0 & -\frac{B'}{2} & 0 & \cdots & \cdots & 0 \\ \vdots & \ddots & \ddots & \ddots & & \vdots \\ \vdots & & \ddots & \ddots & \ddots & \vdots \\ 0 & \cdots & \cdots & 0 & -\frac{B'}{2} & 0 \\ 0 & \cdots & \cdots & \cdots & 0 & -0 \end{pmatrix}$$

$$\vec{Q}_{average} = \frac{1}{2} \begin{bmatrix} \begin{pmatrix} 0 \\ {}^{D}Q'^{n+1}_{end-1} + {}^{D}Q'^{n}_{end-1} \\ \vdots \\ {}^{D}Q'^{n+1}_{2} + {}^{D}Q'^{n}_{2} \\ {}^{D}I^{n+1}_{input} \end{pmatrix} \\ \begin{pmatrix} 0 \\ {}^{U}Q'^{n+1}_{2} + {}^{U}Q'^{n}_{2} \\ \vdots \\ {}^{U}Q'^{n+1}_{end-1} + {}^{U}Q'^{n}_{end-1} \\ {}^{U}I^{n+1}_{input} \end{pmatrix} \end{bmatrix}.$$

The last step before numerical implementation of the scheme is to choose a resolution for the space-time grid. This is an important decision which can influence the stability and/or accuracy of our scheme. To achieve this, we use the convergence condition by Courant-Friedrichs-Lewy. To assure the stability of explicit numerical schemes, the Courant number

$$CFL = v\frac{\Delta t}{\Delta s} \tag{3.44}$$

needs to be < 1. However, our scheme is an implicit scheme. In the case of implicit schemes, stability is always insured and the CFL can be > 1. But a too large CFL can affect accuracy. How big the number can be before errors become too important depends on the scheme, and is interesting to investigate as a high value of CFL reduces greatly computational time. We have found that a value of $CFL = 64$ still assures good accuracy for our scheme. As can be seen in figure 3.3a, the relative difference between $CFL = 1$ and $CFL = 64$ on the upward current flux, used here as a proxy for the intensity of the upward electron flux, falls under 4% after $t = 0.015$ s marked by the dotted line. The greater relative difference before $t = 0.015$ s is due to the value of the flux being close to zero and will not affect our magnetosphere (see figure 3.3b,c). As can be seen by comparing the absolute difference and relative difference, the "true" error on our response is less than 1.5%, which we consider reasonable regarding the huge decrease in computing time.

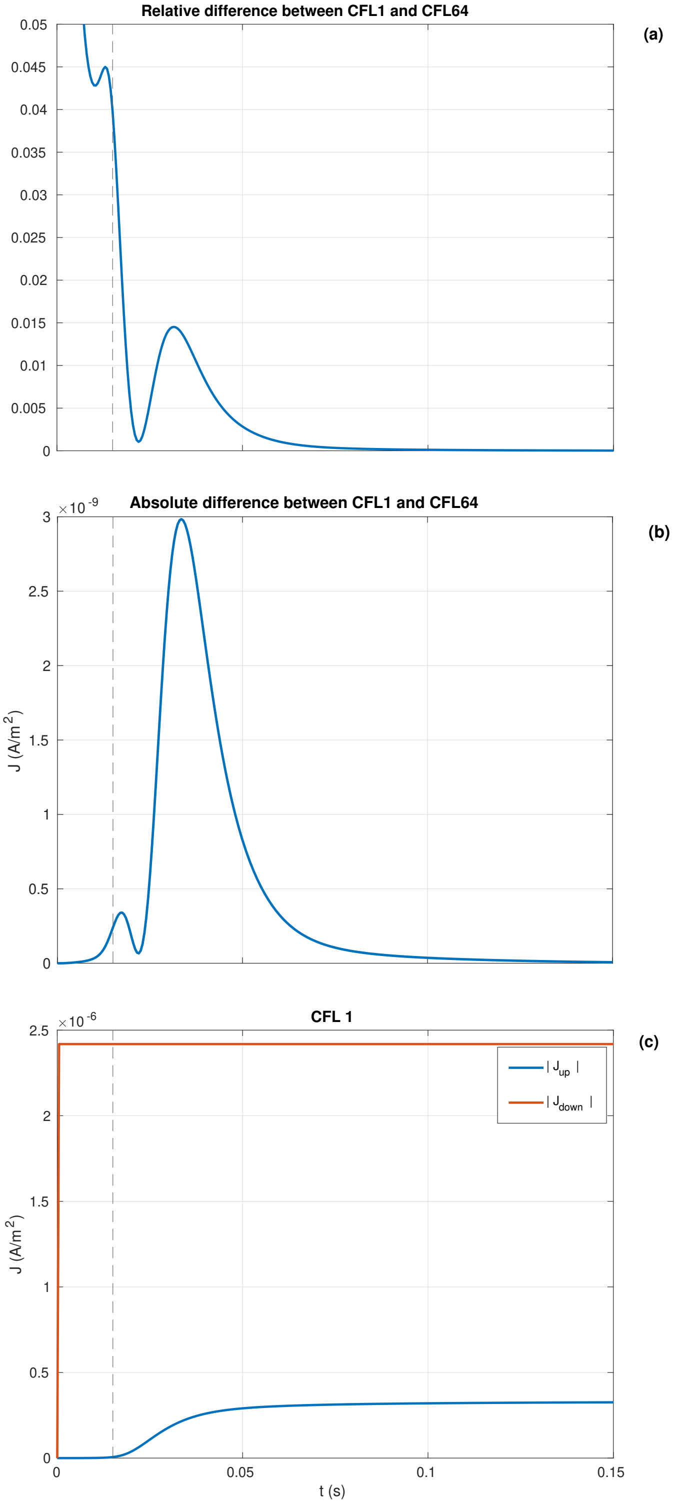

Figure 3.3: **(a,b)** Relative and absolute difference between the currents coming out of the ionosphere for a run with CFL = 1 and a run with CFL = 64. We used a constant precipitation of electrons with a Gaussian in energy centered on 3keV and a width of 100eV. The precipitating electrons were isotropically distributed between a pitch-angle of 0 and 10°. **(c)** Currents in and out of the ionosphere for the run with CFL = 1. In both panels, the vertical dotted line marks the time $t = 0.015$ s.

4

Magnetosphere - Ionosphere coupling

Now that we have reviewed the key elements of both the Vlasov simulations of the acceleration region in chapter 2 and the electron-transport model for the ionosphere in chapter 3, we are now going to see how these two systems are connected in this work. The modified codes for the coupling of the systems are to be found in the GitHub repositories of each model at https://github.com/egavazzi/AURORA and https://github.com/egavazzi/ketchup, under the folders *MI_coupling*.

4.1 Protocol

Our goal is to investigate the effects that a time-dependent ionospheric response could have on the acceleration region. The perfect and most accurate way to do this would be to compute the response from the ionosphere at each time step of the Vlasov simulation, updating the incoming and outcoming flux at the top of the ionosphere continuously. However, this procedure leads to two problems. The first one is that the transport model used here takes several hours on a small super-computer to model 0.35 s of time-dependent ionospheric response. Computing the response over a few minutes while simultaneously integrating the electrostatic Vlasov-Maxwell equations for the the double layer would be extremely computer-time consuming. The second, more practical, is that both models are coded in different languages, making it complicated if not impossible to make them run in parallel and communicate with each other at each time step. Solving this second problem would require a long job of straight re-writing and/or translating of the codes.

The second one is that the transport model used here takes several hours on a small super-computer to model 0.35 s of time-dependent ionospheric response. Computing the response over a few minutes while simultaneously modelling the double layer would be extremely computer-time consuming.

To stay within the limits of what is possible both time-wise and computer-wise, we designed a simplified experiment as follow:

1. We run the Vlasov simulation of the acceleration region for a few minutes without ionospheric response until a double layer appears and steady state is reached. Then, the simulation is stopped and we extract the downward flux of electrons at the ionospheric end of the system at the final time t_{end}.

2. We use this downward flux of electrons as a constant input at the top of the ionosphere in the electron-transport model. The transport model is run with this input until a steady state is reached, which takes approximately 0.35 s. The calculated upward going electron flux is our ionospheric response.

3. We resume the Vlasov simulation from time t_{end} and run it for 0.35 s using the newly obtained ionospheric response as an input at the ionospheric boundary. The downward going electron flux is extracted again but this time over the whole 0.35 s. We run the electron-transport model for 0.35 s with this new time-varying input and obtain a new ionospheric response.

4. We repeat step 3 until the ionospheric response does not change between the runs.

The reason why we repeat step 3 is that the effects the ionospheric response might have on the acceleration region will also change the input into the ionosphere which we considered as constant for the first run. After several run, we might eventually reach a situation where the electron fluxes at the top of the ionosphere

$$I_e^{i+1}(z_{top}, E, \mu, t) = I_e^{i}(z_{top}, E, \mu, t) \tag{4.1}$$

and the electric field in the acceleration region

$$E_z^{i+1}(z,t) = E_z^i(z,t) \tag{4.2}$$

where the superscript i indicates the number of the run. In that case, the system has converged to a solution for the acceleration region response to dynamic ionospheric electron fluxes.

To implement the experiment described above, a transition altitude between the two systems has to be selected, and the data between the two systems converted.

4.2 Transition altitude

The two systems are based on a statistical description of the underlying dynamics, solving equations derived from the Boltzmann equation. However, they solve them in two different physical regimes. The most important difference being that the physics of the Vlasov simulations are governed by the electric and magnetic fields, ignoring particles collisions, while the physics of the electron-transport model are based on particle collisions, ignoring the effects of electric and magnetic fields. Hence, the position of the transition region between the two systems has to be where the transition between the two regimes occurs. We selected 400km for this transition, based on the electron-transport model outputs, where changes in upward fluxes become negligible above 400km (see figure 4.1).

4.3 Conversions of distribution functions and fluxes

Connecting the two systems will require some conversions of data to be made. In principle, both models compute the variation of the phase-space density over one spatial dimension along the magnetic field line and two velocity dimensions. However, the acceleration region model follows variation of the electron velocity distribution function, while the electron-transport model follows variations of the electron flux. One can be found from the other, but it requires some transformations. The transformations have to take into account that the two models use different velocity grids, as one model uses a grid made of $(v_{\|}, \mu_m)$ while the other one uses a grid made of (E, μ_θ).

As an output from the Vlasov simulation, at the ionospheric end, we have the

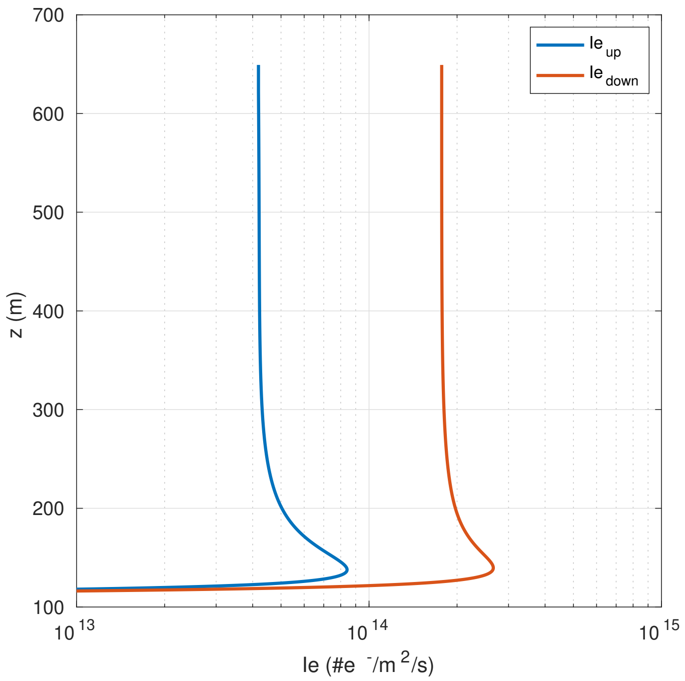

Figure 4.1: Downward and upward electron fluxes through the atmosphere at steady-state. Run with a constant precipitation of electrons with a Gaussian in energy centered on 3keV and a width of 100eV. The changes in fluxes are negligible above 400km where the collision frequencies are small.

distribution function $f_{in}(v_{\|}, \mu_m)$ in $(\#e^- \cdot s^3/m^6)$ given over the velocity grid $(v_{\|}, \mu_m)$. To be able to use it as an input at the top of the ionosphere in the electron-transport model, we need to convert it into a flux of electrons $I_{in}(E, \mu_\theta)$ in $(\#e^-/m^2/s)$ over the grid (E, μ_θ). This is done in steps, first by converting the distribution function into a flux of electron over the same velocity grid $(v_{\|}, \mu_m)$:

$$I_{in}(v_{\|}, \mu_m) = v(v_{\|}, \mu_m) f_{in}(v_{\|}, \mu_m) \Delta v_{\|} \Delta \mu_m \tag{4.3}$$

where $v_{\|}$ and μ denote the middle of the velocity bins, while $\Delta v_{\|}$ and $\Delta \mu$ denote the width of the velocity bins. The total velocity $v(v_{\|}, \mu_m)$ is given by

$$v(v_{\|}, \mu_m) = \sqrt{v_{\|}^2 + \frac{2B}{m}\mu_m}. \tag{4.4}$$

The flux $I_{in}(v_{\|}, \mu_m)$ given over the grid $(v_{\|}, \mu_m)$ is then calculated over the grid (E, μ_θ) simply by calculating for each bin in the old grid the corresponding position in the new grid. Note that several bins in the old grid might correspond to the same bins in the new grid, in which case we need to add the fluxes (see figure 4.2). The energy positions in the new grid are calculated using

$$E = \frac{1}{2}mv^2 = \frac{1}{2}m(v_{\|}^2 + \frac{2B}{m}\mu_m) \tag{4.5}$$

and the pitch-angle cosine

$$\mu_\theta = cos(\theta) = cos(atan\left(\frac{|v_\perp|}{v_{\|}}\right)) = cos(atan\left(\frac{\sqrt{\frac{2B}{m}\mu_m}}{v_{\|}}\right)). \tag{4.6}$$

The new flux $I_{in}(E, \mu_\theta)$ can then be used in the electron-transport model. Once the upgoing flux of electrons $I_{out}(E, \mu_\theta)$ flowing out of the ionosphere is calculated, a similar procedure is used to convert it into the distribution function $f_{out}(v_{\|}, \mu_m)$, first changing grids, and then converting using

$$f_{out}(v_{\|}, \mu_m) = \frac{I_{in}(v_{\|}, \mu_m)}{v(v_{\|}, \mu_m)\Delta v_{\|}\Delta \mu}. \tag{4.7}$$

Note that when we convert the distribution function obtained from the Vlasov simulation to a flux of electron to use in the ionosphere, we obtain some fluxes of electrons at very high energies, due to the $(v_{\|}, \mu_m)$ extending to speed close to the speed of light. However, for double layer with a potential of a few keV, the fluxes at these high energies are extremely small, if not negligible. Taking into account these electrons would require a very large grid in energy for the electron-transport model, which requires a lot of computing time. To avoid unnecessary use of computing power, we cut the energy grid where 99.99 % of the total incoming energy flux is contained.

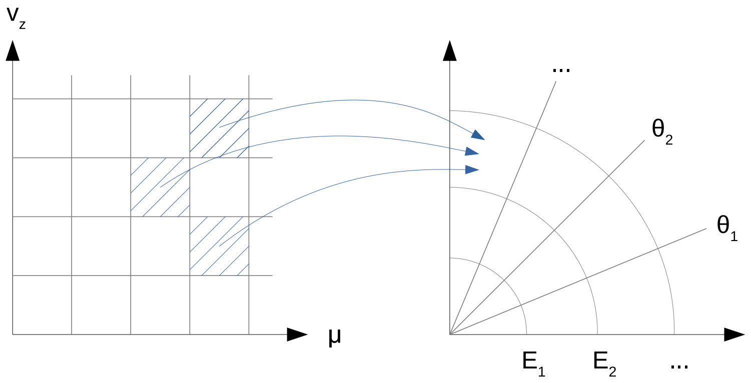

Figure 4.2: Schema of the change of grid between $(v_{||}, \mu_m)$ and (E, μ_θ), where $\mu_\theta = cos(\theta)$. We schematised here a configuration where several bins, here represented in blue in the old grid, correspond to one and same bin in the new one, where the three blue arrows converge.

Using the method described above, a problem quickly appears when changing grids from $(v_{||}, \mu_m)$ to (E, μ_θ). The problem being that the grid used in the Vlasov simulation is coarser than the grid used in the electron-transport model, leading to big discontinuities in energy, as can be seen in figure 4.3a. Running the Vlasov simulation over a finer grid would be very time-consuming and would not have significant effect on the acceleration region. Instead, we refine the grid manually by cutting each bin in smaller pieces. Each subdivision of a bin gets attributed the same distribution function as the original bin. This smooths out the discontinuities in energy when changing grid (see figure 4.3b).

One concern with this method is that electrons from different bins of the grid $(v_{||}, \mu_m)$ can end up in the same bin of the grid (E, μ_θ). When going back to the $(v_{||}, \mu_m)$ grid after having calculated the ionospheric response, electrons from different $(v_{||}, \mu_m)$ bins ends up in only one bin. Total flux is conserved, but is shifted in the grid. To reduce this loss of information, it is important to choose a fine enough (E, μ_θ) grid, especially the size of the pitch-angle streams. We have done some tests where a distribution function is extracted at the ionospheric end from the Vlasov simulation, and is converted into a flux of electron over the new grid. Then, the exact same flux is converted back into the distribution function over the original grid. The final distribution function can be compared to the original one. We did this for different width of pitch-angle bins, and the results are shown in table 4.1. As expected, the test where the shift of flux is minimum is the one where the width of the θ bins is the smallest. However, running the electron-transport code with many streams becomes very time consuming. For this reason, we have chosen to run the electron-transport code with 18 streams, corresponding to a width of pitch-angle bins of 10°. Note that

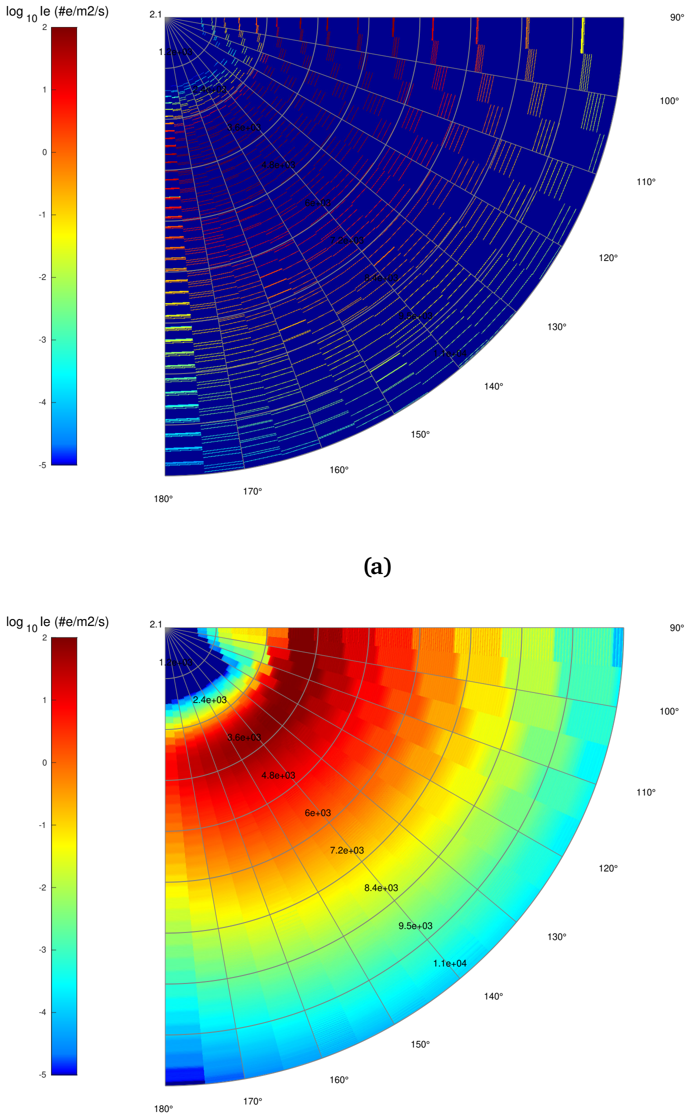

(a)

(b)

Figure 4.3: **(a)** Flux of electrons over the (E, μ_θ) grid after conversion from a distribution function given over the original grid $(v_\parallel, \mu_m)$. **(b)** Flux of electrons over the (E, μ_θ) grid after conversion from the same distribution function but where each bin of the original grid $(v_\parallel, \mu_m)$ has been subdivided in 400 smaller pieces.

Number of streams	θ-width	Flux changing bin
180 streams	1°	3.59 %
36 streams	5°	7.25 %
18 streams	10°	9.98 %
12 streams	15°	12.14 %
10 streams	18°	14.74 %

Table 4.1: Proportion of electron flux changing bin after a back and forth change of grid, as a function of the width of the θ bins

this should not have a big impact on the results since almost all flux changing bin will move to adjacent bins, and total flux is conserved.

5

Results

We have used the protocol described in section 4.1 to study the effects of the time-dependent ionospheric response on the acceleration region. The results are presented in this chapter.

To first obtain a double layer configuration, we run the Vlasov simulation model from Gunell et al. (2013) without the ionospheric response from the electron-transport code. As described in chapter 2, both magnetic field configuration and the densities and temperatures of the different plasma species at the boundaries of the system are of importance for the appearance and stability of double layers. The magnetic field configuration is explained in section 2.2.2, and for plasma characteristics at the boundaries of the system, we choose exactly the same parameters as used by Gunell et al. (2013), since we know they lead to the formation of stable double layers. The distributions function for the ions and electrons at the magnetospheric end are given as a Maxwellian with densities and energies corresponding to an auroral cavity (Gunell et al., 2015b). At the ionospheric end, a Maxwellian is also applied, with temperatures corresponding to a heated upper ionosphere. We summarise these parameters in table 5.1.

The Vlasov simulation is first run with an $\epsilon_r = 4.98 \text{ x } 10^8$ during 10 s without any potential applied between the boundaries of the system, this to allow the system to fill up with particles. Then, the applied potential at the ionospheric boundary is linearly increased from $U = 0$ V to $U = 3$ keV during 20 s. We then keep the potential of 3 keV and run the system until steady state is reached,

	Magnetosphere	Ionosphere
z	0	5.2 x 10^7 m
B	0.086 μT	34 μT
$k_B T_e$	500 eV	1 eV
$k_B T_H^+$	2500 eV	1 eV
n	3 x 10^5 m^{-3}	1 x 10^9 m^{-3}
U	0	3 keV

Table 5.1: Boundary conditions of our acceleration region

which takes around 200 s. After that, we reduce our artificial dielectric constant to $\epsilon_r = 1.27$ x 10^7 and continue to run the system until steady state, which takes around 120 s. With an $\epsilon_r = 1.27$ x 10^7 and the densities chosen at the boundaries, our plasma frequency is reduced (see section 2.2.3) so that the plasma period is approximately equal to 0.013 s. This is an order of 10 times smaller than the time-scale of our ionospheric response. As the time-scale over which plasma properties are changing is greater than the plasma period, effects from the time-dependent ionospheric response on the system should be properly modelled by our simulation.

At steady state and before plugging in the ionospheric response, we have a double layer at around 4.8×10^7 m, corresponding to an altitude of around 4000 km above the ionosphere up along the magnetic field. Figure 5.1 shows the potential and the electric field along the whole magnetic flux tube. Around 2/3 of the rise in potential is confined to a small region, corresponding to the double layer. Figure 5.2 shows also the electric field along the whole magnetic flux tube but as a z-t diagram, during the 0.35 s corresponding to the time window where we are going to plug-in an ionospheric response. We see the stable double layer corresponding to a sharp gradient in the electric field around 4.8×10^7 m.

Using the protocol described in section 4.1, the system made of the ionosphere and the acceleration region converges towards a solution after 3 runs of the ionospheric response, as can be seen in figure 5.3. The absolute difference between the fluxes from the third and the fourth runs are presented in figure 5.4. We consider that a difference in fluxes coming out of the ionosphere of less than 10 $e^-/m^2/s$ is sufficient, in the scope of this work, to claim convergence.

By looking at the fluxes of electrons and energy from the converged solution of the third run (figure 5.3 and figure 5.5), we can understand the electron transport dynamics. First, we observe a sudden rise in both the electron and energy fluxes coming out of the ionosphere between $0 - 0.1$ s, corresponding to scattered high energy primary electrons. After 0.1 s, the upward fluxes start

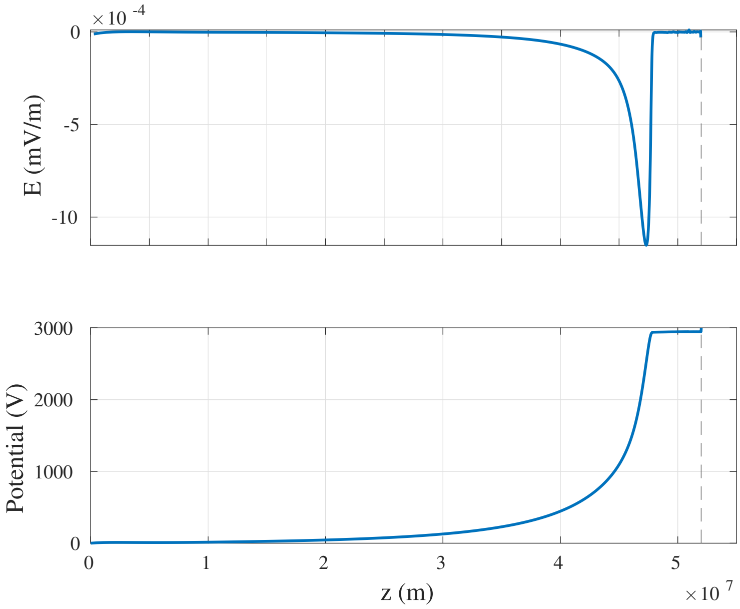

Figure 5.1: Electric field and potential along our magnetic flux tube for steady state conditions (after 120 s at $\epsilon_r = 1.27 \times 10^7$). The negative dip in the electric field corresponds to an upward electric field, accelerating magnetospheric electrons into the ionosphere. The vertical dotted line marks the ionospheric end of the system.

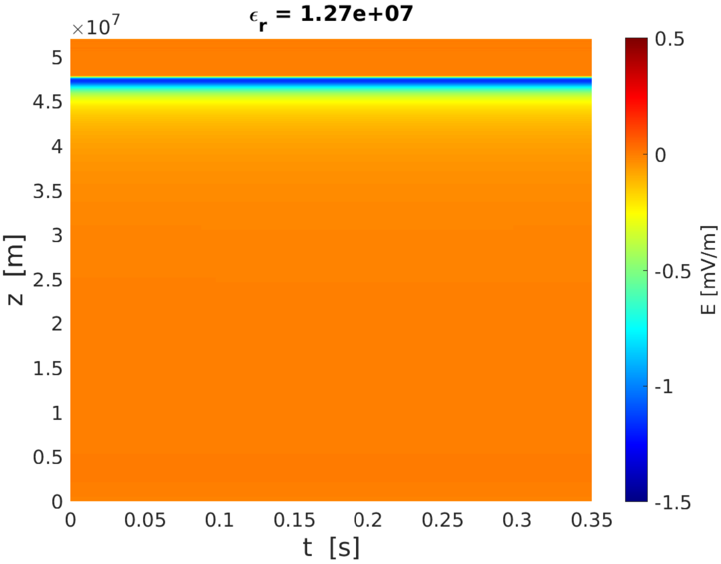

Figure 5.2: Electric field over time and space for no ionospheric response, over the whole magnetic flux tube. The double layer is clearly visible around 4.8×10^7 m

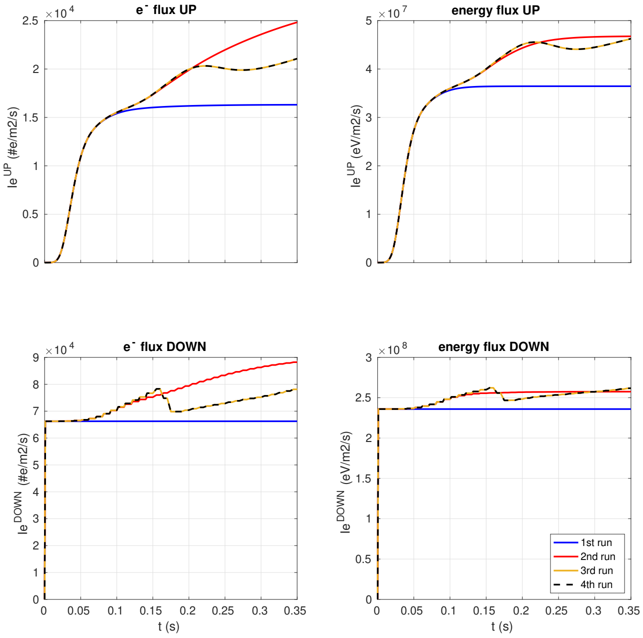

Figure 5.3: Fluxes of electron and energy in and out of the ionosphere for the different runs

to flatten out but then increase again to a plateau around 0.2 s. This second increase corresponds to electrons from the first burst of upward flux that have been reflected back down towards the ionosphere by the double layer potential. This increase is not as large as the first since the primary electrons with a parallel energy $m_e v_{\|}^2/2$ greater than the double layer potential could cross the structure and move towards the magnetotail. This is visible in the panels of figure 5.5 corresponding to the field aligned electrons, with a gap between the very high energies corresponding to magnetospheric electrons streaming down, and slightly lower energies corresponding to electrons from the first response that were reflected. For higher pitch-angles, the fluxes are more continuous in energy. This is due to the higher perpendicular velocity and lower parallel velocity of the electrons, not sufficient for them to cross the double layer. Their path along the magnetic field line is also longer, and is the reason for the more slow and steady rise in energy flux we see after 0.2 s. At $t \approx 0.17$ s, a sudden decrease in the flux of electrons and energy coming down into the ionosphere is visible in figure 5.3 and 5.5. This might be due to the perturbation in the electric field induced by the first burst of upward flux. The sudden perturbation of the potential can move the altitude at which electrons will get mirrored by the double layer higher up, leading to a temporary decrease of the electron flux coming down.

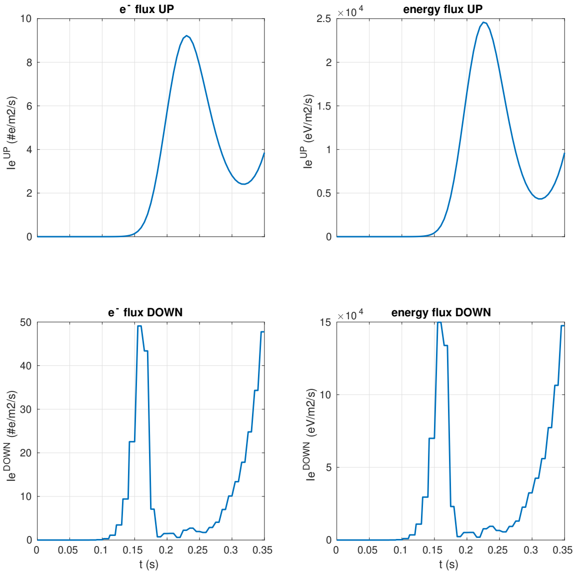

Figure 5.4: Absolute difference between the fluxes in and out of the ionosphere from the 3rd and 4th run.

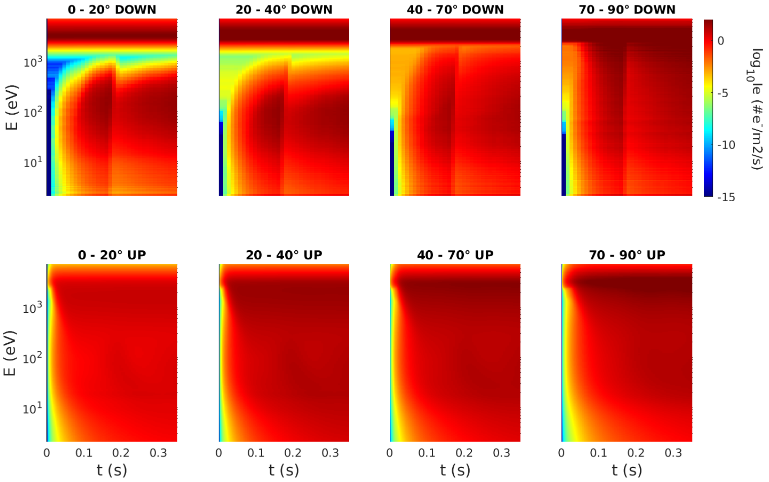

Figure 5.5: Energy and time diagrams of the fluxes of electrons in and out of the ionosphere for the converged solution, for different pitch-angles θ.

The simulations of the acceleration region with the ionospheric response are presented in 5.6. The panel **(a)** corresponds to the acceleration region with no ionospheric response and is presented for comparison. Stable small-scale structures situated between the double layer and the ionosphere are visible, and might be due to the electric field not being totally at steady state. The panel **(b)** and **(c)** correspond to the runs with the first and second ionospheric response, respectively. It is the input at the ionospheric end from panel **(c)** that is used as an input in the third ionospheric response run which is converging to a solution. Because it is converging to a solution in response to this input, the response from the third run does not have significant effects on the acceleration region. Thus, panel **(c)** can be seen as the final converged state of the acceleration region. We can see a negative perturbation of the electric field starting from the ionosphere around $t = 0.05$ s and streaming towards the double layer. This perturbation coincide with the onset of the ionospheric response and the associated sudden burst of back-scattered electrons. Its propagation speed is approximately 2×10^7 m/s, which corresponds to 1200 eV electrons. The perturbation seems to be damped by the narrow structures but eventually reaches the double layer. In reaction, the sharp gradient at the interface of the double layer smooths out slightly, before reverting back to its original shape. Between the double layer and the ionosphere, the electric fields oscillates in response to the first perturbation. But due to the short duration of our experiment, it is hard to conclude on the impact these oscillating structures have on the double layer.

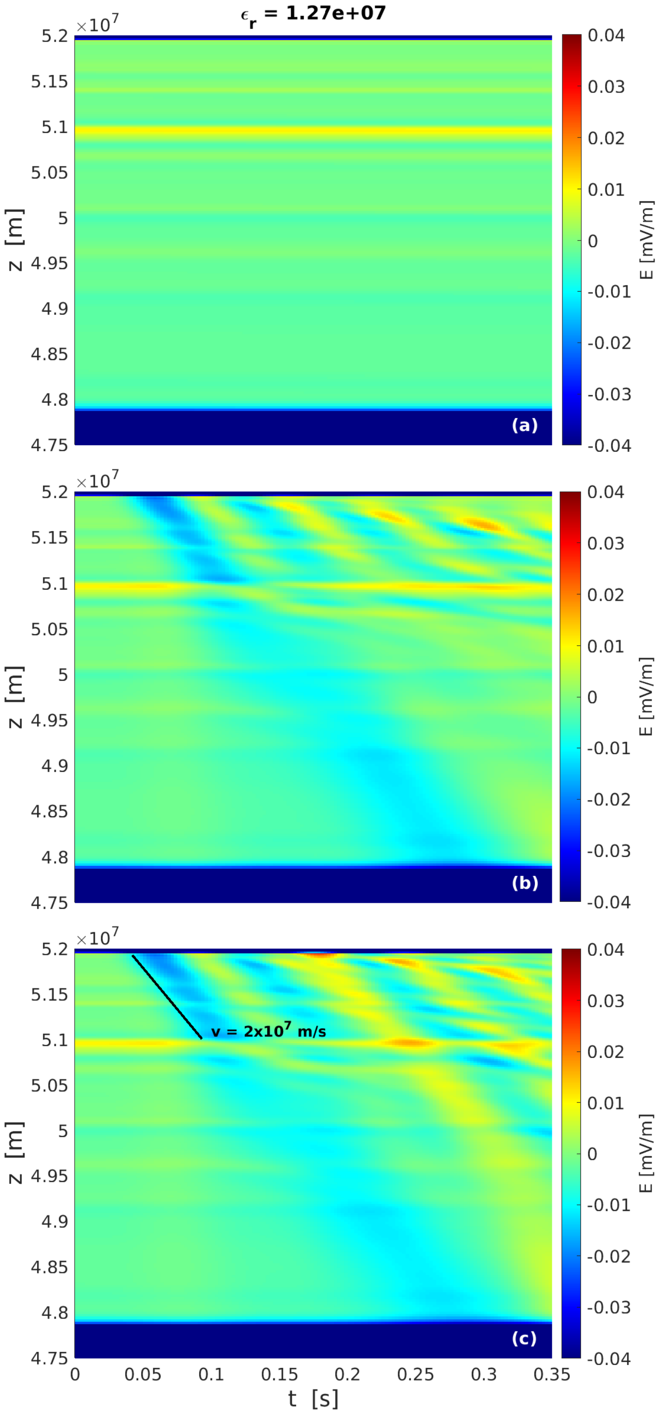

Figure 5.6: Electric field over time and space, zoomed on the ionospheric end, for **(a)** with no ionospheric response, **(b)** with the first ionospheric response, and **(c)** with the second ionospheric response.

/6

Discussions

With our experiment, we have simulated the onset of a time-dependent ionospheric response on a stable double layer. We have found that although the stability of the acceleration structure does not seem to be affected, the sudden onset of the upflow of electrons from the ionosphere response leads to oscillations in the electric field that can be interpreted as electrostatic waves. However, limitations to these results come from that our experiment was simulating a sudden onset and not a continuous ionospheric response, and over a short time interval of 0.35 s.

As we found that our protocol is converging towards a solution and is therefore capable to produce physically valid results, it would be interesting to try variations of the experiment. For example, one could be waiting longer for the double layer to stabilise to avoid the horizontal structures that damped the waves in our experiment and see if the reaction at the double layer interface is different. One could also try to reduce the dielectric constant to see what effects the response might have on the waves observed on the electron timescale by Gunell et al. (2013). Finally, it could be interesting run the experiment for a longer time and for different potential drops.

On a wider scope, because of the electrostatic waves we seem to observe, it would also be interesting to study the effects of a time-dependent ionospheric response for more dynamic situations, e.g. the formation of the potential structure, or for a changing voltage as in the paper by Gunell et al. (2015b). However, this would require some re-writing and translating of the codes to be able to run both systems in parallel for a long time, as explained in section 4.1. Finally, it would be of interest to study the effects of the time-dependent ionospheric response on other acceleration region models, notably simulations of electrostatic potentials and Alfvénic supported electric fields.

Bibliography

Alfvén, H. (1958). On the theory of magnetic storms and aurorae. *Tellus*, *10*, 104–116. https://doi.org/10.1111/j.2153-3490.1958.tb01991.x

Birn, J., Artemyev, A., Baker, D., Echim, M., Hoshino, M., & Zelenyi, L. (2012). Particle acceleration in the magnetotail and aurora. *Space science reviews*, *173*(1), 49–102.

Borovsky, J., Birn, J., Echim, M., Fujita, S., Lysak, R., Knudsen, D., Marghitu, O., Otto, A., Watanabe, T.-H., & Tanaka, T. (2019). Quiescent discrete auroral arcs: A review of magnetospheric generator mechanisms. *Space Science Reviews*, *216*. https://doi.org/10.1007/s11214-019-0619-5

De Keyser, J., & Echim, M. (2010). Auroral and sub-auroral phenomena: An electrostatic picture. *Annales Geophysicae*, *28*(2), 633–650. https://doi.org/10.5194/angeo-28-633-2010

Echim, M. M., Roth, M., & De Keyser, J. (2007). Sheared magnetospheric plasma flows and discrete auroral arcs: A quasi-static coupling model. *Annales Geophysicae*, *25*(1), 317–330. https://doi.org/10.5194/angeo-25-317-2007

Filbet, F., Sonnendrücker, E., & Bertrand, P. (2001). Conservative numerical schemes for the vlasov equation. *Journal of Computational Physics*, *172*(1), 166–187. https://doi.org/https://doi.org/10.1006/jcph.2001.6818

Gronoff, G., Simon Wedlund, C., Mertens, C., & Lillis, R. (2012). Computing uncertainties in ionosphere-airglow models: I. electron ux and species production uncertainties for mars. *Journal of Geophysical Research*, *117*. https://doi.org/10.1029/2011JA016930

Guio, P. (1998). *Studies of ionospheric parameters by means of electron plasma lines observed by EISCAT* (Theses) [ISBN: 8290487924, 9788290487923]. Université Joseph-Fourier - Grenoble I. https://tel.archives-ouvertes.fr/tel-00481443

Gunell, H., Andersson, L., De Keyser, J., & Mann, I. (2015a). Self-consistent electrostatic simulations of reforming double layers in the downward current region of the aurora. *Annales Geophysicae*, *33*(10), 1331–1342. https://doi.org/10.5194/angeo-33-1331-2015

Gunell, H., Andersson, L., De Keyser, J., & Mann, I. (2015b). Vlasov simulations of trapping and loss of auroral electrons. *Annales Geophysicae*, *33*(3), 279–293. https://doi.org/10.5194/angeo-33-279-2015

Gunell, H., De Keyser, J., Gamby, E., & Mann, I. (2013). Vlasov simulations of parallel potential drops. *Annales Geophysicae*, *31*(7), 1227–1240. https://doi.org/10.5194/angeo-31-1227-2013

Khazanov, G., Neubert, T., & Gefan, G. (1994). A unified theory of ionosphere-plasmasphere transport of suprathermal electrons. *IEEE Transactions on Plasma Science*, *22*(2), 187–198. https://doi.org/10.1109/27.279022

Lummerzheim, D., & Lilensten, J. (1994). Electron transport and energy degradation in the ionosphere: Evaluation of the numerical solution, comparison with laboratory experiments and auroral observations. *12*(10), 1039–1051.

Lysak, R., Echim, M., Karlsson, T., Marghitu, O., Rankin, R., Song, Y., & Watanabe, T.-H. (2020). Quiet, discrete auroral arcs: Acceleration mechanisms. *Space Science Reviews*, *216*(5), 92. https://doi.org/10.1007/s11214-020-00715-5

Marklund, G., Johansson, T., Lileo, S., & Karlsson, T. (2007). Cluster observations of an auroral potential and associated field-aligned current reconfiguration during thinning of the plasma sheet boundary layer. *Journal of Geophysical Research: Space Physics*, *112*(A1). https://doi.org/https://doi.org/10.1029/2006JA011804

Marklund, G. T. (1997). Auroral phenomena related to intense electric fields observed by the freja satellite. *Plasma Physics and Controlled Fusion*, *39*(5A), A195–A226. https://doi.org/10.1088/0741-3335/39/5a/020

Marklund, G., Ivchenko, N., Karlsson, T., Fazakerley, A., Dunlop, M., Lindqvist, P., Buchert, S., Owen, C., Taylor, M., Vaivalds, A., Carter, P., André, M., & Balogh, A. (2002). Temporal evolution of the electric field accelerating electrons away from the auroral ionosphere. *Nature*, *414*, 724–7. https://doi.org/10.1038/414724a

Peticolas, L., & Lummerzheim, D. (2000). Time-dependent transport of field-aligned bursts of electrons in flickering aurora. *Journal of Geophysical Research*, *105*, 12895–12906. https://doi.org/10.1029/1999JA000398

Sato, N., Nakamura, M., & Hatakeyama, R. (1986). Three-dimensional double layers inducing ion-cyclotron oscillations in a collisionless plasma. *Phys. Rev. Lett.*, *57*, 1227–1230. https://doi.org/10.1103/PhysRevLett.57.1227

Schunk, R., & Nagy, A. (2009). Simplified transport equations. *Ionospheres: Physics, plasma physics, and chemistry* (2nd ed., pp. 113–158). Cambridge University Press. https://doi.org/10.1017/CBO9780511635342.005

Sivukhin, S. (1965). *Reviews of plasma physics, vol. 1*. New York Consultants bureau.

Solomon, S. C. (1993). Auroral electron transport using the monte carlo method. *Geophysical research letters*, *20*(3), 185–188.

Solomon, S. C. (2001). Auroral particle transport using monte carlo and hybrid methods. *Journal of Geophysical Research: Space Physics*, *106*(A1), 107–116. https://doi.org/https://doi.org/10.1029/2000JA002011

Song, B., D'Angelo, N., & Merlino, R. L. (1992). Stability of a spherical double layer produced through ionization. *Journal of Physics D: Applied Physics*, *25*(6), 938–941. https://doi.org/10.1088/0022-3727/25/6/006

Swartz, W. E., Nisbet, J. S., & Green, A. E. S. (1971). Analytic expression for the energy-transfer rate from photoelectrons to thermal-electrons. *Journal of Geophysical Research (1896-1977)*, *76*(34), 8425–8426. https://doi.org/https://doi.org/10.1029/JA076i034p08425